Marine and Petroleum Geology 113 (2020) 104166

Contents lists available at ScienceDirect

Marine and Petroleum Geology

journal homepage: www.elsevier.com/locate/marpetgeo

Research paper

Quantification of gas hydrate saturation and morphology based on a generalized effective medium model

Haojie Pan[a,b], Hongbing Li[a], Jingyi Chen[b], Michael Riedel[c], Melanie Holland[d], Yan Zhang[a,*], Shengjuan Cai[a]

[a] Department of Geophysical Technology, Research Institute of Petroleum Exploration and Development, 100083, Beijing, China
[b] Seismic Anisotropy Group, Department of Geosciences, The University of Tulsa, 74104, Tulsa, United States
[c] GEOMAR, Helmhotz Center for Ocean Research, Kiel, Germany
[d] Geotek Ltd., 4 Sopwith Way, Daventry, NN11 8PB, United Kingdom

ARTICLE INFO

Keywords:
Hydrate morphology
Hydrate saturation
Generalized effective medium model
Modified cementation theory
Elastic wave velocities

ABSTRACT

Numerous models have been developed for prediction of gas hydrate saturation based on the microstructural relationship between gas hydrates and sediment grains. However, quantification of hydrate saturation and morphology from elastic properties has been hindered by failing to account for complex hydrate distributions. Here, we develop a generalized effective medium model by applying the modified Hashin-Shtrikman bounds to a newly developed cementation theory. This model is validated by experimental data for synthetic methane and tetrahydrofuran hydrates. Good comparison of model predictions with experimental measurements not only reveals its ability to merge the results of contact cementation theory and effective medium theory, but also indicates its feasibility for characterizing complex morphologies. Moreover, the results of inverting acoustic measurements quantitatively confirm that for synthetic samples in "excess-gas" condition gas hydrates mainly occur as a hybrid-cementing morphology with a low percentage of pore-filling morphology, whereas for pressure-core hydrate-bearing sediments in natural environments they exist as matrix-supporting and pore-filling morphologies with a very low percentage of hybrid-cementing morphology. The hydrate saturations estimated from sonic and density logs in several regions including northern Cascadia margin (Integrated Ocean Drilling Program Expedition 311, Hole U1326D and Hole U1327E), Alaska North Slope (Mount Elbert test well) and Mackenzie Delta (Mallik 5L-38), are comparable to the referenced hydrate saturations derived from core data and resistivity, and/or nuclear magnetic resonance log data, confirming validity and applicability of our model. Furthermore, our results indicate that ~8% hybrid-cementing, ~33% matrix-supporting and ~59% pore-filling hydrates may coexist in the fine-grained and clay-rich marine sediments on the northern Cascadia margin, whereas ~10% hybrid-cementing, ~54% matrix-supporting and ~36% pore-filling hydrates may coexist in the coarse-grained and sand-dominated terrestrial sediments of the Alaska North Slope and Mackenzie Delta.

1. Introduction

Gas hydrates are naturally occurring ice-like crystalline solids formed under low-temperature and high-pressure conditions, which are found along continental margins and in terrestrial permafrost regions (Sloan, 1998). In recent years, gas hydrates have received worldwide interest due to their potential as a promising major future energy resource and their possible impacts on climate change and seafloor stability (Riedel et al., 2010).

The presence of gas hydrates alters the physical properties of host sediments significantly by increasing seismic wave velocities (Chand et al., 2004). The effect of hydrates on seismic wave velocities is not only dependent on hydrate saturation but also on the microstructural distribution of hydrate grains within host sediments, which may include morphologies such as contact-cementing, grain-coating, pore-filling, matrix-supporting, matrix-inclusion and fracture-filling (Ecker et al., 1998; Helgerud, 2001; Dai et al., 2004). These morphologies frequently coexist in natural hydrate-bearing sediments. For example, gas hydrates that occur as pore-filling and vein/fracture-filling with possible matrix-supporting or grain-coating morphologies have been reported in the Krishna-Godavari Basin and South China Sea (Qian et al., 2017; Holland et al., 2018; Yoneda et al., 2018; Collett et al., 2019), while pore-filling, matrix-supporting and grain-coating morphologies have been found at the Mallik site on the Meckenzie Delta (Dai et al., 2008; Winters et al.,

* Corresponding author.
E-mail addresses: panhj88@petrochina.com.cn (H. Pan), zya@petrochina.com.cn (Y. Zhang).

https://doi.org/10.1016/j.marpetgeo.2019.104166
Received 17 July 2019; Received in revised form 5 December 2019; Accepted 5 December 2019
Available online 10 December 2019

2014). Except for seismic wave velocities, hydrate morphology is also strongly correlated with other physical properties of gas hydrate-bearing sediments, such as seismic wave attenuation, permeability, shear strength, electrical resistivity and thermal conductivity (Priest et al., 2006; Chand et al., 2006; Ellis, 2008; Cortes et al., 2009; Dai et al., 2012; Best et al., 2013; Delli and Grozic, 2014; Katagiri et al., 2017; Yoneda et al., 2018; X. Liu et al., 2018; Pan et al., 2019c; Sahoo et al., 2019). Thus, a good knowledge of gas hydrate morphology in host sediments is essential for improving the accuracy of hydrate saturation estimation and lowering the risks in gas hydrate exploitation.

Investigation of hydrate morphology is crucial for modeling the elastic behaviors of hydrate-bearing sediments and for better understanding the gas hydrate deposit environments, as well as for revealing the hydrate occurrence mechanism. Laboratory experiments on the formation of synthetic hydrates, or direct observation of natural hydrate-bearing sediments recovered in pressure are often used to study the microscopic characteristics of gas hydrate occurrences (Holland et al., 2008; Hu et al., 2012; Chaouachi et al., 2015; Yang et al., 2016; Jin et al., 2016; Sahoo et al., 2018). Such studies suggest that hydrates exhibit different morphologies in different formation conditions; for instance, hydrates mainly occur as contact-cementing or grain-coating morphologies in “excess-gas” (gas saturated pore space) conditions, while they form as matrix-supporting or pore-filling morphologies in “excess-water” (water saturated pore space) (e.g., natural environments) conditions (Priest et al., 2005; Dugarov et al., 2019). Recently, advances in pressure coring techniques and analysis have allowed in situ measurement of hydrate saturation and examination of hydrate morphology in natural gas hydrate-bearing sediments (Rydzy, 2014; Schindler et al., 2017; Holland et al., 2018). However, pressure-core samples are rare, potentially mechanically disturbed and expensive (Dai and Santamarina, 2014; Cook and Waite, 2018). Although logging-while-drilling resistivity images (Cook et al., 2014; Kim et al., 2013; Collett et al., 2019) can be used to identify and differentiate pore-filling and vertical or sub-vertical fracture-filling hydrates, they are unable to detect vein/nodular-filling hydrates and fractures with small dip angles. Crossplots of P- and S-wave velocities versus hydrate saturation (Dai et al., 2004, 2008; Pan et al., 2019c) are a common tool to diagnose the morphology of gas hydrates from well-log and experimental data, but this method depends on a variety of models which assume that gas hydrates are mainly present as a single morphology in host sediments and which may yield differing results. These methods fail to quantify the fractions of multiple hydrate morphologies and capture the spatial occurrence mechanism of hydrates on a seismic or basin-wide scale. Therefore, there is a need for improved methods for the precise detection and characterization methods of complex hydrate morphologies.

Numerous theoretical models that refer to hydrate morphology have been developed to predict gas hydrate saturation (Dvorkin and Nur, 1996; Helgerud et al., 1999; Lee et al., 1996; Jakobsen et al., 2000; Chand et al., 2004, 2006; Lee and Waite, 2008; Lee and Collett, 2009; Zhang et al., 2013; Sriram et al., 2014; Jaiswal et al., 2014; Z. Liu et al., 2018; Terry and Knapp, 2018; Nguyen-Sy et al., 2019; Pan et al., 2019a). For example, the contact cementation theory (CCT) (Dvorkin and Nur, 1996) has been often used to characterize contact-cementing and grain-coating hydrates, and the effective medium model (EMM) (Dvorkin et al., 1999; Helgerud et al., 1999) has been used to quantify the amount of pore-filling and matrix-supporting hydrates. Additionally, the combined self-consistent approximation (SCA) and differential effective medium (DEM) theory is used to delineate the cementing and matrix-inclusion hydrate-bearing sediments (Chand et al., 2006; Minshull and Chand, 2009). However, these models can be applied to two morphologies at most, as they are based on the assumption that gas hydrates are either present in cementing form (contact-cementing and grain-coating) or non-cementing form (pore-filling, matrix-supporting, and matrix-inclusion). The unified contact cementation theory combines the cementing and non-cementing morphologies (Pan et al., 2019a), but it could not allow for grain-coating and contact-cementing morphologies simultaneously. That is to say, existing models are unable to delineate more complex hydrate morphologies. Therefore, a more general model is required to reliably quantify hydrate saturation and complex morphologies from elastic properties.

In this study, we first develop a modified cementation theory based on general expressions of pressure-dependent normalized contact-cemented radii and approximate expressions of the normal and tangential stiffnesses between contact-cemented and Hertzian-contact scenarios. We then propose a generalized effective medium model (GEMM) by applying the modified Hashin-Shtrikman upper and lower bounds to the novel cementation theory at critical porosity. We validate the feasibility of this model with two sets of laboratory experimental data for synthetic methane and tetrahydrofuran (THF) hydrates. Next, we apply the proposed model to quantify the fractions of multiple hydrate morphologies and analyze the possible hydrate occurrence mechanism from the acoustic measurements of synthetic hydrate samples and natural recovered pressure-core hydrate samples. Finally, we predict hydrate saturation and fractions of multiple morphologies at Site U1326 and Site U1327 (Integrated Ocean Drilling Program (IODP) Expedition 311, northern Cascadia margin) and the Mount Elbert test well (Alaska North Slope), as well as at Mallik 5L-38 (Mackenzie Delta) (Fig. 1).

2. Theory

The CCT (Dvorkin and Nur, 1996) and EMM (Dvorkin et al., 1999; Helgerud et al., 1999) are frequently used to characterize hydrate-bearing sediments. However, the CCT is independent of effective pressure and poorly suited for low-porosity cemented rocks; moreover, it cannot couple with the Hertz-Mindlin theory (Mindlin, 1949) if the cement content is equal to zero. To overcome the drawbacks of the CCT and merge it with EMM, we derive a GEMM by applying the modified Hashin-Shtrikman bounds to a modified cementation theory. In this section, we will provide the detailed derivation of pressure-dependent normalized contact-cemented radii and modified cementation theory, as well as GEMM.

2.1. Pressure-dependent normalized contact-cemented radii

To allow for the impact of effective pressure on the elastic properties, we assume that two identically spherical grains with radius R have a finite circle contact area instead of point contact (assumption of CCT) with initial contact radius a_0 under the effective pressure P_{eff} (Dvorkin and Yin, 1995; Elata and Dvorkin, 1996), and cement accumulates at the grain contacts (contact-cementing), coats on grain surfaces (grain-coating), or coexists at grain contacts and on grain surfaces (hybrid-cementing). This assumption accounts for some aspects of rock texture (e.g. grain angularity and sorting to some extent) and the issue of diagenesis (e.g. mechanical compaction and cementation). For simplicity, the geometrical relationships between grains (blue) and cement (yellow) for three arrangements can be illustrated in Fig. 2. Based on the expressions of normalized contact-cemented radii derived by Pan et al. (2019a, equations (1) and (2)), we can obtain the pressure-dependent normalized contact-cemented radii for contact-cementing and grain-coating cases by setting the thickness of cement layer to 0.

If cement accumulates at grain contacts as shown in Fig. 2(a), the normalized contact-cemented radius α can be expressed as

$$\alpha = \sqrt{\alpha_0^2 + \sqrt{\frac{16}{3n}\frac{(\varphi_c - \varphi)}{(1 - \varphi_c)}}} \tag{1}$$

where α_0 is the initial normalized contact radius with $\alpha_0 = \frac{a_0}{R} = \left[\frac{3\pi(1-\nu_{ma})P_{eff}}{2n(1-\varphi_c)G_{ma}}\right]^{\frac{1}{3}}$ (Mavko et al., 2009); φ and φ_c are the effective and critical porosities, respectively. n is the coordination number

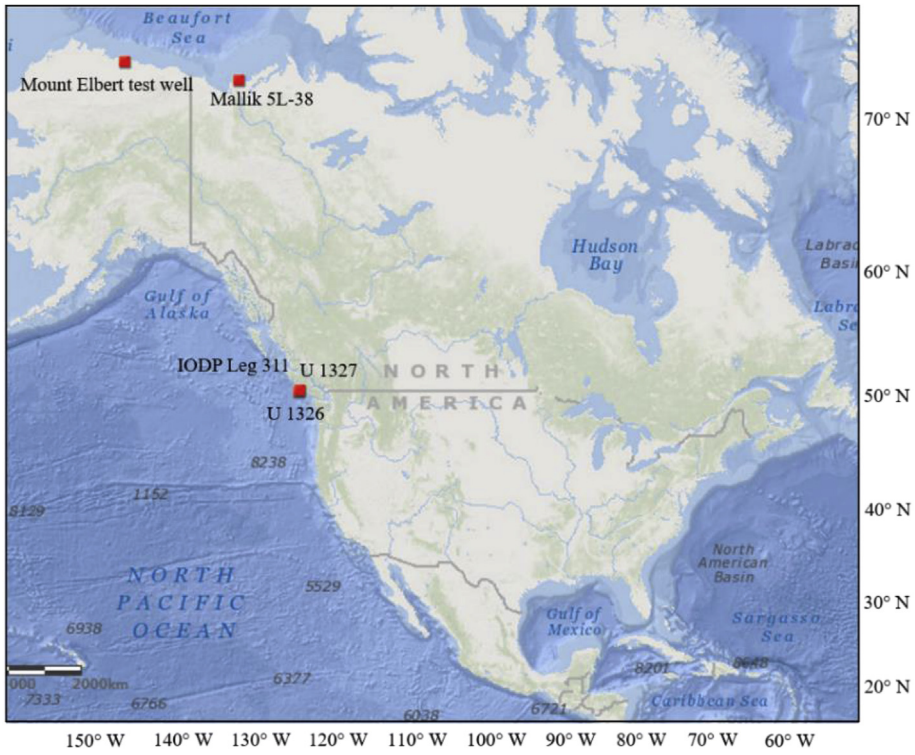

Fig. 1. The location of well sites. (a): two permafrost-associated gas hydrate research wells: the Mallik 5L-38 research well in Mackenzie Delta and Mount Elbert test well in Alaska North Slope. (b): two sites from IODP: Site U1326 and Site U1327. Bathymetry source: Esri (ArcGIS).

(average number of grain contacts per grain); G_{ma} and ν_{ma} are the shear modulus and the Poisson's ratio of the matrix, respectively.

If cement distributes evenly around the grain surface as shown in Fig. 2(b), the normalized contact-cemented radius α can be written as

$$\alpha = \sqrt{\alpha_0^2 + \frac{2(\varphi_c - \varphi)}{3(1-\varphi_c)}} \tag{2}$$

Based on expressions of equations (1) and (2), the normalized contact-cemented radius for hybrid-cementing case (Fig. 2(c)) can be yielded as

$$\alpha = \sqrt{\alpha_0^2 + \left[\frac{[2n(1-W_c)+16W_c](\varphi_c-\varphi)}{3n(1-\varphi_c)}\right]^{\frac{2-W_c}{2}}} = \sqrt{\alpha_0^2 + \left[\frac{[2n(1-W_c)+16W_c]\varphi_c S_c}{3n(1-\varphi_c)}\right]^{\frac{2-W_c}{2}}} \tag{3}$$

where S_c is the cementing hydrate saturation which is equivalent to $S_{gh}f_c$, f_c is the fraction of hybrid-cementing morphology; W_c is defined as the weighted cement factor which ranges from 0 to 1. Here, $W_c = 0$ and $W_c = 1$, respectively, represent the grain-coating and contact-cementing cases.

As the effective pressure tends to zero, equations (1)–(3) respectively reduce to the normalized contact-cemented radii as

$$\beta = \sqrt[4]{\frac{16(\varphi_c-\varphi)}{3n(1-\varphi_c)}} \tag{4}$$

$$\beta = \sqrt{\frac{2(\varphi_c-\varphi)}{3(1-\varphi_c)}} \tag{5}$$

$$\beta = \sqrt{\left[\frac{[2n(1-W_c)+16W_c](\varphi_c-\varphi)}{3n(1-\varphi_c)}\right]^{\frac{2-W_c}{2}}} = \sqrt{\left[\frac{[2n(1-W_c)+16W_c]\varphi_c S_c}{3n(1-\varphi_c)}\right]^{\frac{2-W_c}{2}}} \tag{6}$$

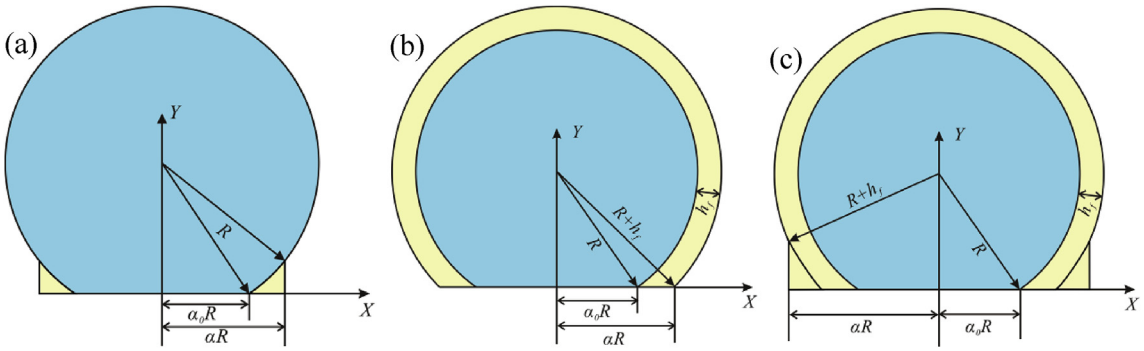

Fig. 2. Schemes for the three configurations between the cement (yellow) and grains (blue): a) contact-cementing; (b) grain-coating; (c) hybrid-cementing. (For interpretation of the references to colour in this figure legend, the reader is referred to the Web version of this article.)

Note that equations (4) and (5) are the same as the classic contact-cemented radii proposed by Dvorkin et al. (1999) and equation (6) is equivalent to the normalized contact-cemented radius for intermediate scheme derived by Allo (2019). The pressure-dependent normalized contact-cemented radii will be simplified into the initial normalized contact radius α_0 if the cement content is equal to zero.

2.2. Modified cementation theory

Starting from the equations of CCT, Langlois (2015) proposed approximate expressions of the normal (D_N) and tangential (D_T) stiffnesses between the contact-cemented scenario and the Hertzian-contact scenario in the "rigid cement" regime (where the maximal stress is located at the periphery), given as,

$$D_N = \frac{4G_{ma}b}{(1-\nu_{ma})(1+f(A_N))} \tag{7}$$

$$D_T = \frac{8G_{ma}b\left(1+\frac{\nu_{ma}}{2-\nu_{ma}}g(A_T)\right)}{(2-\nu_{ma})[1+f(A_T)]} \tag{8}$$

where $b=\beta R$, $A_N=\beta/\Lambda_N$ and $A_T=\beta/\Lambda_T(1-\nu_{ma}/2)$ $\Lambda_N=G_c(1-\nu_{ma})/\pi G_{ma}$, $\Lambda_T=G_c/\pi G_{ma}$, $M_c=2G_c(1-\nu_c)/(1-2\nu_c)$. b is the normalized contact-cemented radius; β is the classic normalized contact-cemented radius which can be calculated using equation (6). $G_c$and$\nu_c$are the shear modulus and the Poisson's ratio of the cement, respectively. The corrective functions are expressed as

$$f(A_N) = 0.3092A_N^{0.9098}\frac{0.1036A_N^{0.4139}+1}{A_N^{0.4139}+1} \tag{9}$$

$$f(A_T) = 0.3092A_T^{0.9098}\frac{0.1036A_T^{0.4139}+1}{A_T^{0.4139}+1} \tag{10}$$

$$g(A_T) = \frac{-0.428A_T^{0.4189}}{1+1.336A_T^{1.222}+4.031A_T^{0.523}} \tag{11}$$

It should be noted that the normal and tangential stiffnesses and the corrective functions are only related to the classic normalized contact-cemented radii β.

As interactions of contact and cementation between cement and grain coexist in grain contact area, it is more appropriate to use the pressure-dependent normalized contact-cemented radii. Therefore, the contact-cemented normal (S_N) and tangential (S_T) stiffnesses can be modified as

$$S_N = \frac{4aG_{ma}}{(1-\nu_{ma})(1+f(A_N))} \tag{12}$$

$$S_T = \frac{8aG_{ma}}{2-\nu_{ma}}\frac{(1+\nu_{ma}/(2-\nu_{ma})\cdot g(A_T))}{1+f(A_T)} \tag{13}$$

where $a=\alpha R$ is the radius of contact-cemented area between two grains.

Then, for a random packing, the effective bulk modulus K_{cct} and shear modulus G_{cct} (Digby, 1981; Winkler, 1983) can be expressed as:

$$K_{cct} = \frac{n(1-\varphi)}{12\pi R}S_N \tag{14}$$

$$G_{cct} = \frac{n(1-\varphi)}{20\pi R}\left(S_N+\frac{3}{2}S_T\right) \tag{15}$$

Substituting equations (12) and (13) into equations (14) and (15) yields

$$K_{cct} = \frac{n(1-\varphi)\alpha G_{ma}}{3\pi(1-\nu_{ma})(1+f(A_N))} \tag{16}$$

$$G_{cct} = \frac{n(1-\varphi)\alpha G_{ma}}{5\pi}\left[\frac{1}{(1-\nu_{ma})(1+f(A_N))}+\frac{3}{2-\nu_{ma}}\frac{1+\nu_{ma}/(2-\nu_{ma})g(A_T)}{1+f(A_T)}\right] \tag{17}$$

where the normalized radii α can be calculated by using equation (3). Note that equations (16) and (17) are pressure-dependent and reduced to the Hertz-Mindlin theory (Mindlin, 1949) when the cement content tends to zero.

2.3. Generalized effective medium model (GEMM)

Dvorkin et al. (1999) proposed an EMM by applying the modified Hashin-Shtrikman bounds (Hashin and Shtrikman, 1963) to the Hertz-Mindlin theory at critical porosity. In the same spirit, we calculate the dry-rock moduli at critical porosity using the proposed cementation theory. Then, the modified Hashin-Shtrikman bounds are employed to obtain the effective dry-rock moduli at arbitrary porosity. Separating into regions above and below critical porosity, the bulk (K_{dry}) and shear (G_{dry}) moduli of dry frame can be expressed as:

$$K_{dry} = \begin{cases} \left[\frac{\varphi/\varphi_c}{K_{cct}+\frac{4}{3}G_{cct}}+\frac{1-\varphi/\varphi_c}{K_{ma}+\frac{4}{3}G_{cct}}\right]^{-1}-\frac{4}{3}G_{cct}, & \varphi<\varphi_c, \\ \left[\frac{(1-\varphi)/(1-\varphi_c)}{K_{cct}+\frac{4}{3}G_{cct}}+\frac{(\varphi-\varphi_c)/(1-\varphi_c)}{\frac{4}{3}G_{cct}}\right]^{-1}-\frac{4}{3}G_{cct}, & \varphi\geq\varphi_c, \end{cases} \tag{18}$$

$$G_{dry} = \begin{cases} \left[\frac{\varphi/\varphi_c}{G_{cct}+Z}+\frac{1-\varphi/\varphi_c}{G_{ma}+Z}\right]^{-1}-Z, & \varphi<\varphi_c, \\ \left[\frac{(1-\varphi)/(1-\varphi_c)}{G_{cct}+Z}+\frac{(\varphi-\varphi_c)/(1-\varphi_c)}{Z}\right]^{-1}-Z, & \varphi\geq\varphi_c, \end{cases} \tag{19}$$

where K_{cct} and G_{cct} represent the effective moduli at critical porosity calculated from the modified cementation theory. K_{ma} is the bulk modulus of the matrix. $Z=\frac{G_{cct}}{6}\left(\frac{9K_{cct}+8G_{cct}}{K_{cct}+2G_{cct}}\right)$. Equations (18) and (19) effectively overcome the issue that CCT is poorly suited for low-porosity cemented rocks. Moreover, they degrade to the EMM (Dvorkin et al., 1999; Helgerud et al., 1999) as cement content tends to zero.

The subsequent saturated bulk (K_{sat}) and shear (G_{sat}) moduli can be calculated from Gassmann's equation (Gassmann, 1951),

$$K_{sat} = K_{ma}\frac{\varphi K_{dry}-(1+\varphi)K_{fl}K_{dry}/K_{ma}+K_{fl}}{(1+\varphi)K_{fl}+\varphi K_{ma}-K_{fl}K_{dry}/K_{ma}} \tag{20}$$

$$G_{sat} = G_{dry} \tag{21}$$

where K_{fl} represents the bulk modulus of pore fluid.

Finally, the elastic wave velocities can be calculated as

$$V_p = \sqrt{\frac{K_{sat}+4/3G_{sat}}{\rho_b}}, V_s = \sqrt{\frac{G_{sat}}{\rho_b}} \tag{22}$$

where ρ_b denotes the bulk density calculated using the volume weighted average method.

3. Methods

3.1. Rock physics modeling of gas hydrate-bearing sediments

Based on the GEMM, rock physics modeling of hydrate-bearing sediments with three hydrate morphologies (see Fig. 3) can be divided into three main parts:

(1) Assuming that gas hydrates become a component of the matrix (Fig. 3(a)), the original porosity φ reduces to $\varphi_e=\varphi(1-S_{gh}f_{ms})$ and the bulk and shear moduli of the matrix are calculated using Hill's average (Hill, 1963) as

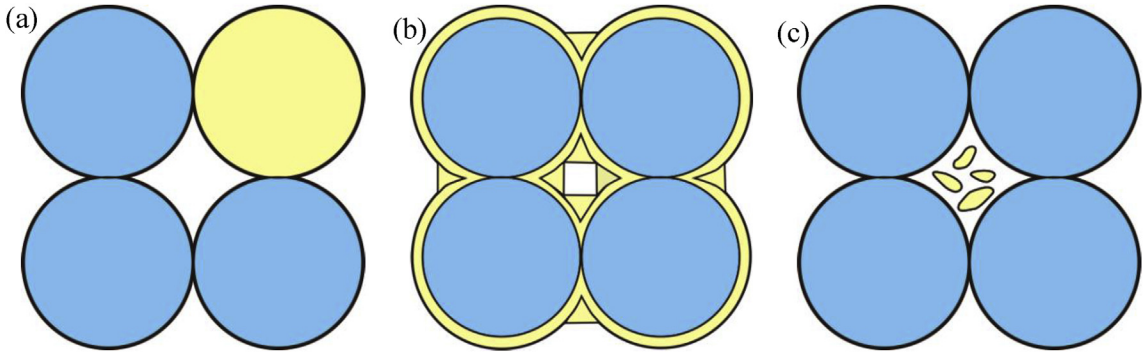

Fig. 3. Three types of hydrate morphologies. (a): matrix-supporting; (b): hybrid-cementing and (c) pore-filling:. Blue spheres represent sediment grains and the yellow refer to hydrates. (For interpretation of the references to colour in this figure legend, the reader is referred to the Web version of this article.)

$$K_{ma} = \frac{1}{2}\left\{f_h K_h + (1-f_h)(1-V_{sh})K_s + (1-f_h)V_{sh} K_{sh} + \left[\frac{f_h}{K_h} + \frac{(1-f_h)(1-V_{sh})}{K_s} + \frac{(1-f_h)V_{sh}}{K_{sh}}\right]^{-1}\right\} \quad (23)$$

$$G_{ma} = \frac{1}{2}\left\{f_h G_h + (1-f_h)(1-V_{sh})G_s + (1-f_h)V_{sh} G_{sh} + \left[\frac{f_h}{G_h} + \frac{(1-f_h)(1-V_{sh})}{G_s} + \frac{(1-f_h)V_{sh}}{G_{sh}}\right]^{-1}\right\} \quad (24)$$

where S_{gh} and f_{ms} are the total hydrate saturation and the fraction of matrix-supporting morphology, respectively; V_{sh} is the clay content. $f_h = (\varphi - \varphi_e)/(1-\varphi_e)$ is the fraction of gas hydrates in the matrix; K_h,K_s, K_{sh} are the bulk moduli of hydrates, quartz and clay, respectively. G_h, G_s and G_{sh} are the shear moduli of hydrates, quartz and clay, respectively.

(2) Since contact-cementing and grain-coating hydrates mainly affect the stiffnesses of the dry-rock frame, the GEMM can be used to calculate the dry-rock moduli. Unlike the approach adopted by Marín-Moreno et al. (2017), we calculate the effective elastic moduli of hydrate-bearing sediments containing hybrid-cementing morphologies (Fig. 3 (b)) by introducing a weighted cement factor. Different values of weighted cement factor represent different combinations of grain-coating and contact-cementing morphologies. We have to bear in mind that the porosity in Gassmann's equation (equations (20) and (21)) will further reduce to $\varphi_{eff} = \varphi(1 - S_{gh}(f_{ms} + f_c))$ due to the presence of hybrid-cementing hydrates.

(3) Assuming that part of hydrates fills into the pore space (Fig. 3 (c)), the bulk modulus of pore fluid can be calculated using

$$\frac{1}{K_{fl}} = \frac{S_{gh}f_{pf}}{(1 - S_{gh} + S_{gh}f_{pf})}\frac{1}{K_h} + \frac{1 - S_{gh}}{(1 - S_{gh} + S_{gh}f_{pf})}\frac{1}{K_w} \quad (25)$$

where K_w is the bulk modulus of water. f_{pf} is the fraction of pore-filling morphology. Note that the sum of the fractions of hydrate morphologies is equivalent to 1.

3.2. Very fast simulated annealing method

The goal of this study is to quantitatively assess gas hydrate morphology and saturation. To avoid falling into local minimum or relying on starting models, a global optimization method, the very fast simulated annealing (VFSA) algorithm (Ingber, 1989), is employed to predict hydrate saturation and fractions of hydrate morphologies. To obtain reliable and stable solutions from the limited input elastic data (P- and S-wave velocities and density), we set a weighted cement factor to adjust the ratio of grain-coating and contact-cementing morphologies in the hybrid-cementing hydrates and assume that gas hydrates are present as a combination of pore-filling, matrix-supporting and hybrid-cementing morphologies in host sediments. Given the measured P- and S-wave velocities and density, the fractions of hydrate morphologies and hydrate saturation can be predicted by solving a non-linear inverse problem by minimizing the objective function:

$$E = [(V_p^{obs} - V_p^{cal})^2 + (V_s^{obs} - V_s^{cal})^2 + (\rho_b^{obs} - \rho_b^{cal})^2]^{1/2} \quad (26)$$

where V_p^{obs}, V_s^{obs}, ρ_b^{obs} are the observed P- and S-wave velocities and density, respectively. V_p^{cal}, V_s^{cal}, ρ_b^{cal} are the calculated P- and S-wave velocities and density, respectively. After determining the fractions of matrix-supporting and pore-filling morphologies, the fraction of hybrid-cementing morphology can be obtained.

Fig. 4 shows the workflow of the VFSA algorithm for quantification of hydrate saturation and the fractions of pore-filling and matrix-supporting morphologies. First, an initial model $m_i = (S_{gh,i}, f_{ms,i}, f_{pf,i})$ $(0 \le S_{gh,i} \le 1\ 0 \le f_{ms,i} \le 1\ 0 \le f_{pf,i} \le 1$, hydrate saturation and fractions of matrix-supporting and pore-filling morphologies) is selected randomly from the model space $m_i^{\min} < m_i < m_i^{\max}$ and the initial objective function E_i is evaluated. Here, the minimum ($m_i^{\min}$) and maximum ($m_i^{\max}$) values of the initial model are set to be 0 and 1, respectively.

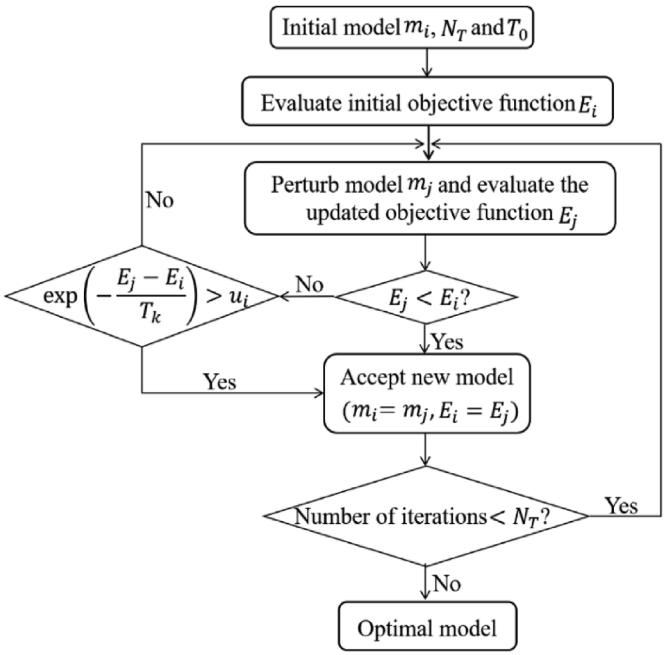

Fig. 4. Workflow of the VFSA algorithm for quantification of hydrate saturation and morphology.

Then, the initial model m_i is updated to a new model m_j using the following equation

$$m_j = m_i + y_i(m_i^{\max} - m_i^{\min}) \quad (27)$$

where $y_i = \mathrm{sgn}(u_i - 0.5)T_k\left[\left(1 + \frac{1}{T_k}\right)^{|2u_i-1|} - 1\right]$, u_i is a random number varying between 0 and 1. i and j are the previous and subsequent iteration numbers in the minimization. $T_k = T_0\lambda^{k-1}$, T_0 is the initial temperature. Here, the constant λ is set to be 0.95. $k$is the number of iterations (1,2,3,$\cdots$,N_T) and N_T is the total number of iterations. For this study, we set the initial temperature and total number of iterations as 100 and 3000, respectively. Next, the objective function E_j for the updated model is calculated and compared with the previous objective function for the previous model. The new model is accepted if $E_j < E_i$ and rejected, or rejected with a probability $p = 1 - \exp\left(-\frac{E_j - E_i}{T_k}\right)$ if$E_j > E_i$. Finally, the optimal model is obtained after completing the predefined largest iterations.

4. Validation of the GEMM model with experimental data

To evaluate the performance of the GEMM, we compare its predictions with those obtained by two other conventional models (EMM and CCT). The input P- and S-wave velocities are measured on unconsolidated sand samples containing synthetic methane and THF hydrates by Dugarov et al. (2019) (Fig. 5). The elastic constants for the sediment constituents used in the calculations are listed in Table 1. The critical porosity, coordination number and effective pressure are 0.4, 9 and 10 MPa (Dugarov et al., 2019), respectively. As we can see, velocities calculated from the GEMM are fully consistent with those from the EMM for pore-filling and matrix-supporting morphologies, and are comparable to those from the CCT for contact-cementing and grain-coating morphologies. In addition, the experimental results demonstrate that most methane hydrate samples follow the trend of multiple morphologies with 84% grain-coating, 12% matrix-supporting and 4% pore-filling, while most THF hydrate samples agree well with the trend of multiple morphologies with 1% grain-coating, 96% matrix-supporting and 3% pore-filling. These comparisons suggest that our model not only effectively merges the results of CCT and EMM, but also captures the multiple morphological characteristics of gas hydrates at microscale during their formation.

Table 1
Bulk modulus, shear modulus and density of sediment constituents.

Component	Bulk modulus (GPa)	Shear modulus (GPa)	Density (g/cm^3)
Quartz[a]	36	45	2.65
Clay[a]	20.9	6.85	2.58
Marine hydrate[b]	6.41	2.54	0.91
Terrestrial hydrate[c]	8.7	3.5	0.92
THF hydrate[b]	7.92	3.25	0.91
Pore water[a]	2.25	0	1
Free gas[d]	0.12	0	0.23

[a] (Lee, 2002).
[b] (Lee et al., 2007).
[c] (Lee and Collett, 2011; Riedel et al., 2014).
[d] (Helgerud et al., 1999).

5. Application to laboratory data

5.1. Quantification of hydrate morphology for synthetic hydrate-bearing sediments

Priest et al. (2005) formed synthetic methane hydrates under "excess-gas" conditions using resonant column setups with suitable temperature and pressure (500 kPa), and measured the P- and S-wave velocities in the seismic frequency range. Here, we first generate the crossplots of P- and S-wave velocities versus hydrate saturation using our GEMM to diagnose possible morphologies for 11 synthetic hydrate samples as shown in Fig. 6. The critical porosity is set to be the mean value of measured initial porosity (~0.42) in the experiment. By fitting the measured P- and S-wave velocities, the coordination number is determined as 6.5. The results indicate that measured P- and S-wave velocities are slightly underestimated by our model at a hydrate saturation of 0–20% although the correlation with the trend of grain-coating morphology is relatively high. This discrepancy between measured and predicted P-wave velocities might be a consequence of neglecting the presence of methane gas in the modeling, or it might imply that hybrid-cementing, pore-filling and matrix-supporting hydrates coexist in the samples. Consequently, we quantify the fractions of these three morphologies directly from the measured P- and S-wave velocities for the given hydrate saturation and porosity for synthetic samples using the VFSA method (Fig. 7) with a weighted cement factor of 0.35. The results indicate that pore-filling hydrates form at the initial stage with extremely low saturations, and hybrid-cementing hydrates occur

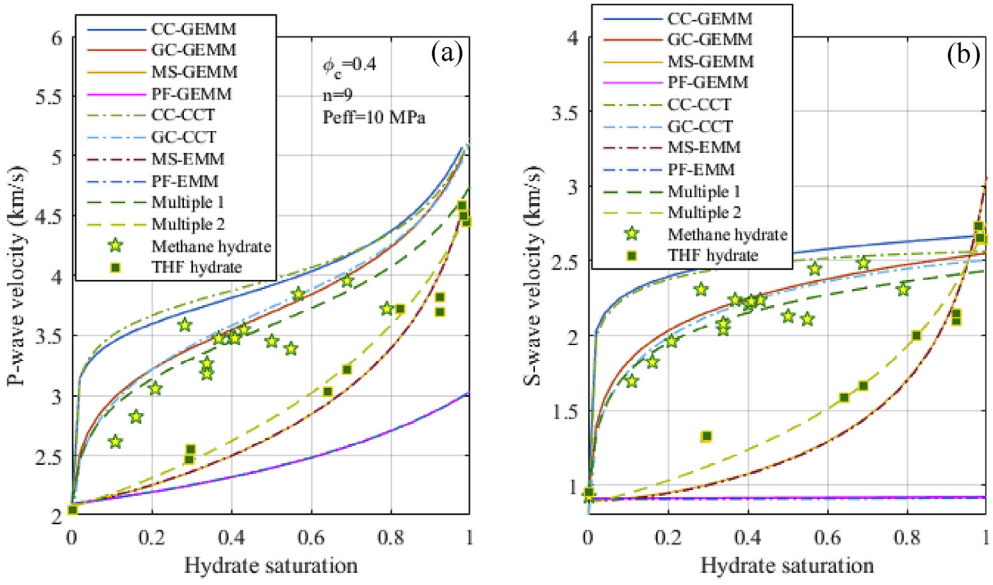

Fig. 5. Comparison of obtained P- (a) and S-wave (b) velocities in samples containing methane (stars) and THF hydrates (squares) (Dugarov et al., 2019) with estimations by GEMM (solid lines), CCT (dash-dotted lines) and EMM (dash-dotted lines). Multiple 1 case (green dashed line) is derived from GEMM with a combination of hydrate morphologies composed by 84% grain-coating (GC), 12% matrix-supporting (MS) and 4% pore-filling (PF); Multiple 2 case (yellow dashed line) is another combination of morphologies with 1% GC, 96% MS and 3% PF. (For interpretation of the references to colour in this figure legend, the reader is referred to the Web version of this article.)

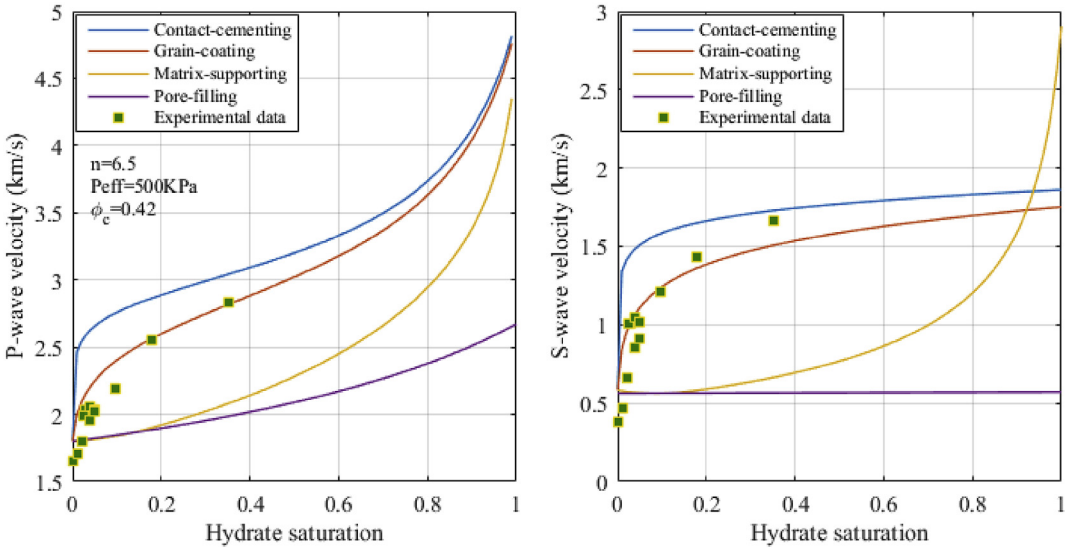

Fig. 6. Crossplots of P- and S-wave velocities versus hydrate saturation for four types of hydrate morphologies. Model predictions (solid lines) for velocities are calculated using the GEMM and the superposed data (green squares) are the experimental data based on synthetic core samples measured by Priest et al. (2005). (For interpretation of the references to colour in this figure legend, the reader is referred to the Web version of this article.)

at around 3% hydrate saturation, and the two coexist at hydrate saturations between 5% and 35%. This is consistent with finding of Priest et al. (2005) that for the "excess-gas" condition hydrates initially cement at sand grain contacts (3%–5% hydrate saturation) then fill into pore space (5%–35% hydrate saturation). This is mainly because hydrates preferentially form where water lies at the gas-saturated condition(Cook and Waite, 2018).

Fig. 7 shows the theoretical effects of hydrate morphologies on P- and S-wave velocities and demonstrates that hybrid-cementing morphology causes a relative increase of S-wave velocity, while pore-filling morphology produces a relative decrease of P-wave velocity. The matrix-supporting morphology creates moderate increases in P- and S-wave velocities. These effects are predominantly caused by the impact of hydrate morphology on elastic behaviors. For instance, pore-filling hydrates are supposed to affect only the pore fluid bulk modulus, whereas matrix-supporting and hybrid-cementing hydrates tend to enhance the elastic moduli of the matrix and dry frame, respectively.

5.2. Quantification of hydrate morphology for natural hydrate-bearing sediment cores

Yoneda et al., 2018b measured the P- and S-wave velocities of the

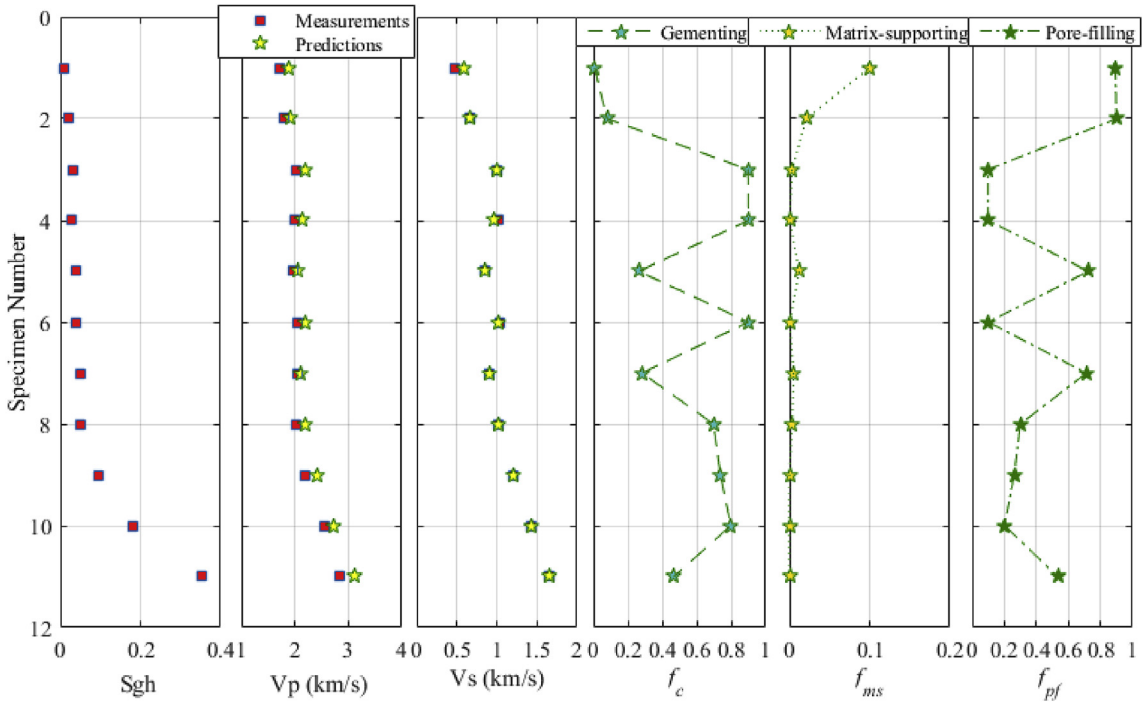

Fig. 7. Fractions of hybrid-cementing, matrix-supporting and pore-filling morphologies estimated from measured elastic-wave velocities using the VFSA for the synthetic core (Priest et al., 2005). From left to right: hydrate saturation, P-wave velocity, S-wave velocity, fraction of hybrid-cementing hydrates, fraction of matrix-supporting hydrates, and fraction of pore-filling hydrates. The measurements and predictions are marked by red squares and stars, respectively. (For interpretation of the references to colour in this figure legend, the reader is referred to the Web version of this article.)

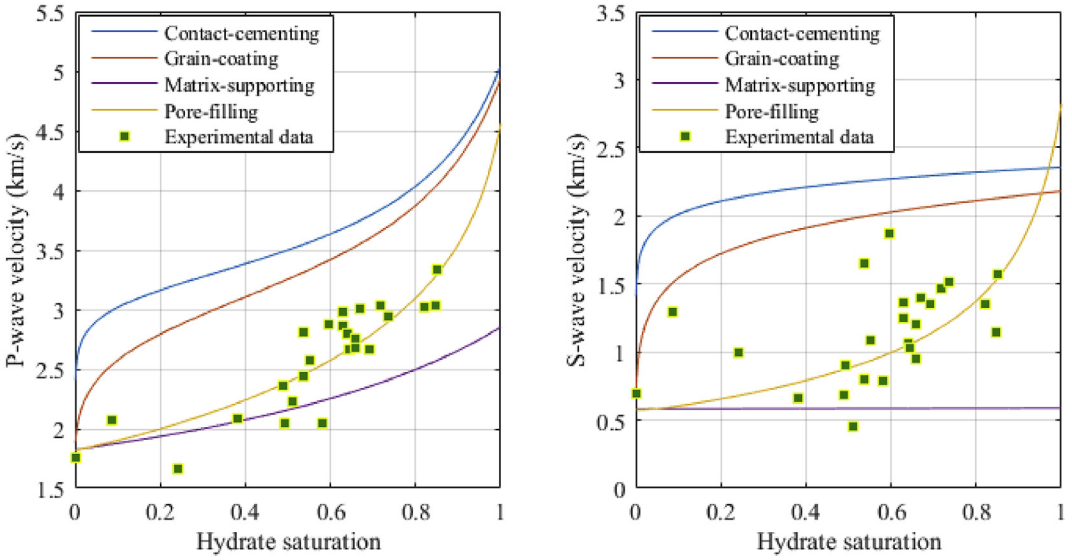

Fig. 8. Crossplots of P- and S-wave velocities versus hydrate saturation for four types of hydrate morphologies. Model predictions (solid lines) for velocities are calculated using the GEMM and the superposed data (green squares) are the experimental data based on pressure core samples measured by Yoneda et al., 2018b. (For interpretation of the references to colour in this figure legend, the reader is referred to the Web version of this article.)

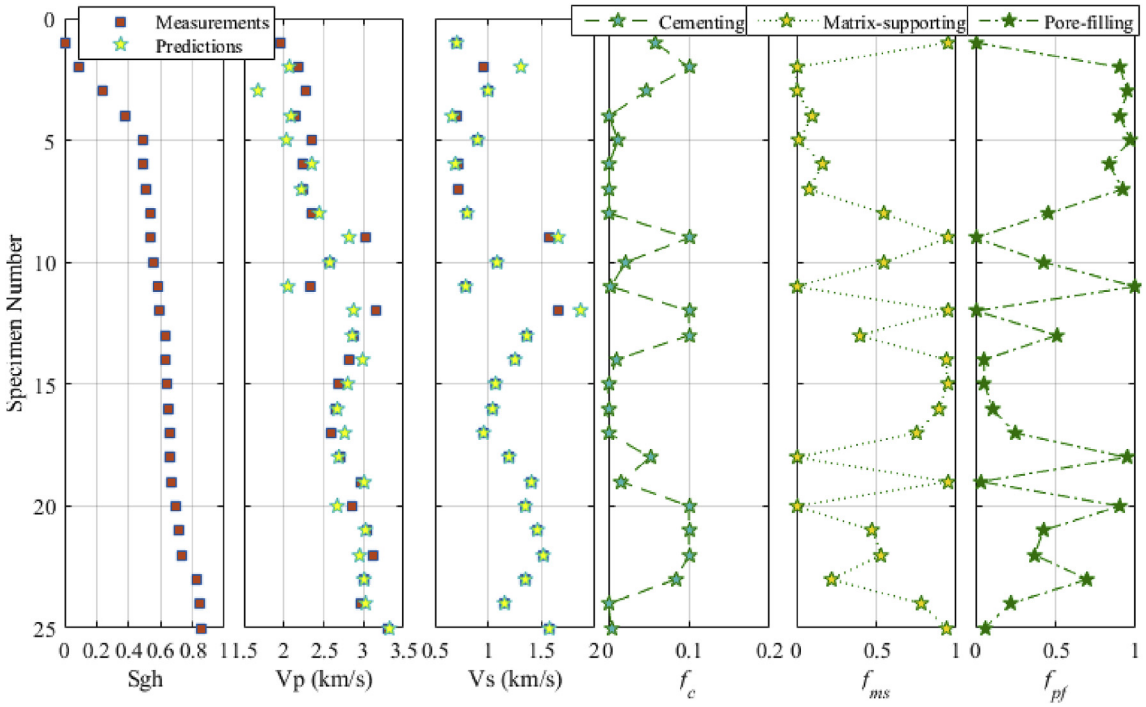

Fig. 9. Fractions of hybrid-cementing, matrix-supporting and pore-filling morphologies estimated from measured elastic-wave velocities using the VFSA for the pressure core samples at the NGHP-02 area (Yoneda et al., 2018b). From left to right: hydrate saturation, P-wave velocity, S-wave velocity, fraction of hybrid-cementing hydrates, fraction of matrix-supporting hydrates, and fraction of pore-filling hydrates. The measurements and predictions are marked by red squares and stars, respectively. (For interpretation of the references to colour in this figure legend, the reader is referred to the Web version of this article.)

pressure-core hydrate-bearing sediments from the Krishna-Godavari Basin with a triaxial testing apparatus. Fig. 8 compares the measured elastic-wave velocities and gas hydrate saturations with the GEMM results. Optimization of the calculated and measured velocities generates a coordination number of 6 and a critical porosity of 0.4. It is found that most of measured data points highly correlate with the trend of matrix-supporting morphology with some of data on the trend of pore-filling or grain-coating morphology (Fig. 8). Hence, based on the measured elastic-wave velocities of the chosen 25 samples, the fractions of these morphologies are also evaluated using the VFSA method with a weighted cement factor of 0.05. Fig. 9 shows that the calculated P- and S-wave velocities agree well with the measured values. Moreover, estimates from the natural core samples reveal a linkage between relative changes in velocities and hydrate morphology similar to that for the synthetic hydrate samples. Compared with synthetic hydrates, the naturally-occurring hydrates from the Krishna-Godavari Basin predominantly fill the pore space at hydrate saturations below 50% and become part of the frame at hydrate saturations above 60%. Small amounts of hybrid-cementing hydrates are also diagnosed in the sediments. This may be because gas hydrates grow at the gas-water

Table 2
Summary information of drill sites used in this study.

Regions	Sites	BGHS depth	Porosity (Mean)	Instrinic permeability	Grain size (μm)	Gas hydrate characteristics	Lithologhy	References
IODP Leg 311, northern Cascadia margin	U1326D	~264 mbsf	0.4–0.6	–	5–15	Pore-filling, disseminated, veins, nodules	Fine-grained clay to silty clay	Riedel et al. (2006); Riedel et al. (2006, 2010a); Holland et al. (2008) Dai et al. (2012).
	U1327E	~230 mbsf	0.4–0.65	–	5–15	Pore-filling, disseminated, veins, nodules	Fine-grained clay or silty clay	
Alaska North Slope	Mount Elbert test well	~869.6 m	0.35–0.42	300–2150 mD	10 ~210	Pore-filling, with possible matrix-supporting	Coarse-grained fine sand	Winters et al. (2011); Lee and Collett (2011).
Mackenzie Delta	Mallik 5L-38	~1110 m	~0.30	100–4000 mD	11 ~337	Matrix-supporting, pore-filling, grain-coating	Coarse-grained sand	Dallimore and Collett (2005); Winters et al. (2005).

interface and then become hydrate grain filling in the pore space (Kingston et al., 2008). The estimates are consistent with semi-quantitative analyses of the mechanical properties, permeability and acoustic velocity for the same samples made by Yoneda et al. (2018a,2018b,2018c) which show that complex morphologies, including matrix-supporting, grain-coating and pore-filling types, might coexist in the Krishna-Godavari Basin.

6. Application to well-log data

6.1. Well-log data from marine and permafrost settings

To compare hydrate saturation and morphology as predicted from our GEMM with those interpreted from well-log and/or core data, we choose four drill sites (Fig. 1) from IODP Expedition 311 (Holes U1326D and U1327E) on the northern Cascadia margin, the Mount Elbert test well on the Alaska North Slope, and Mallik 5L-38 research well at Mackenzie Delta in Canada (see Table 2 for summary information and references). In these areas, gas hydrates have been confirmed from elevated P-wave velocities and resistivity logs, as well as from core samples. Of the four sites, the Mount Elbert and Mallik 5L-38 data sets have the most complete sets of well logs for predicting hydrate saturation. The conventional wireline logging (CWL) data, such as P- and S-wave velocities, Gamma Ray (GR) and resistivity logs were acquired at Hole U1326D and Hole U1327E. Because density logs are absent at Holes U1326D and U1327E, we used density logs measured at nearby wells U1326A and U1327D, situated about 20 m away from the two target wells. Note that the clay content is calculated from GR log and the porosity is derived from density log rather than assuming they are constant. The sample-derived hydrate saturation is obtained from salinity and/or chloride data. At each site, the target intervals for prediction of hydrate saturation and fractions of multiple morphologies are situated within the gas hydrate stability zone (GHSZ). The base of gas hydrate stability (BGHS) in Sites U1326D and U1327E, the Mount Elbert test well and Mallik 5L-38 are located at ~264 m below seafloor (mbsf), ~230 mbsf, ~869.6 m and ~1110 m, respectively (Riedel et al., 2010; Lee and Collett, 2011; Henninges et al., 2005). For simplicity, we assume that the sediment matrix consists of sand and clay, and gas hydrates coexist as pore-filling, matrix-supporting and hybrid-cementing morphologies. For variable parameters, the coordination number and critical porosity are chosen based on the previous studies in the northern Cascadia margin (Pan et al., 2019d) and Mount Elbert test well (Pan et al., 2019b), as well as Mallik 5L-38 well (Riedel et al., 2014). Due to lack of experimental data for calibration of the weighted cement factor, here we suppose it to be 0.1 for the marine sediments and 0.2 for the permafrost-related sediments. The relevant free modeling parameters for the calculations at the four sites are summarized in Table 3.

Table 3
Variable parameters used for the calculations at the selected four sites.

Site	Coordination number	Critical porosity	Weighted cement factor
U1326D [a]	4	0.42	0.1
U1327E [a]	4	0.42	0.1
Mount Elbert [b]	6	0.36	0.2
Mallik 5L-38 [b, c]	6	0.38	0.2

[a] (Pan et al., 2019d).
[b] (Pan et al., 2019).
[c] (Riedel et al., 2014).

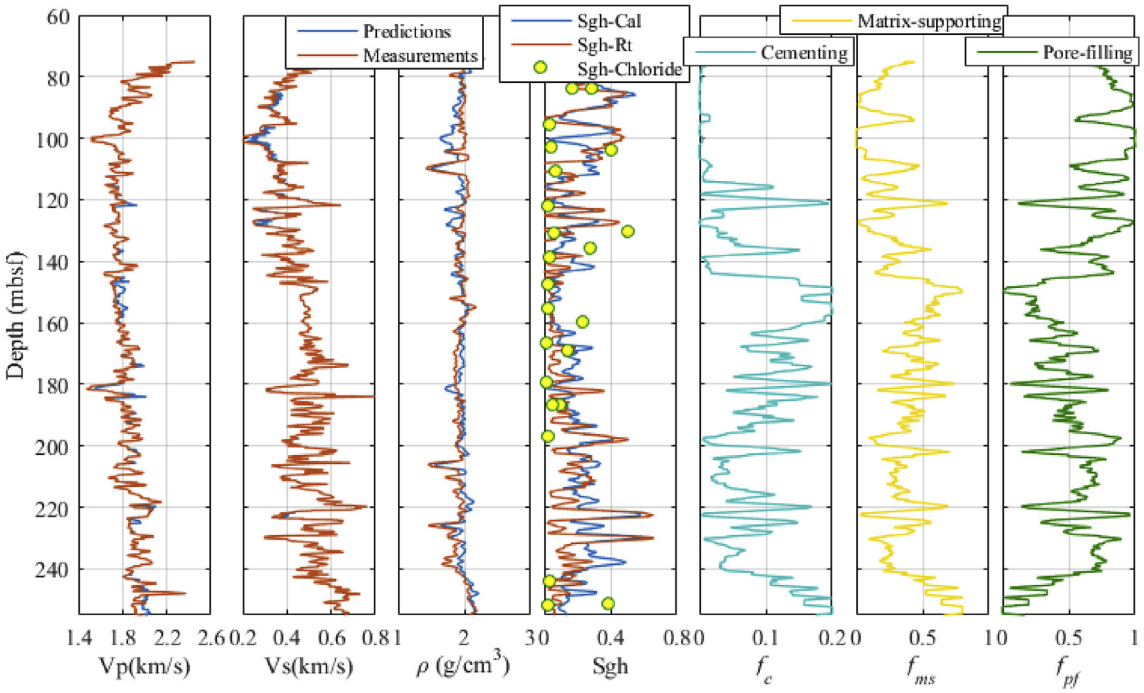

Fig. 10. Inversion results at Site U1326D. From left to right: P-wave velocity, S-wave velocity, density, hydrate saturation, the fractions of hybrid-cementing, matrix-supporting, and pore-filling hydrates. Measured data are in red, predictions with developed model in blue. The hydrate saturation predicted from the GEMM is in blue (Sgh-Cal) and the calculation of hydrate saturation from Rt log is in red (Sgh-Rt). The yellow dots denote the hydrate saturation calculated from chloride data (Sgh-Chloride). All saturations and fractions of hydrate morphologies are smoothed using a 9-point running average. (For interpretation of the references to colour in this figure legend, the reader is referred to the Web version of this article.)

6.2. Quantification of hydrate saturation and morphology for marine hydrate-bearing sediments

6.2.1. IODP expedition 311-hole U1326D

Fig. 10 shows the comparison of interpretations from Site U1326D with hydrate saturation and fractions of hybrid-cementing, matrix-supporting and pore-filling morphologies simultaneously predicted from the measured P- and S-wave velocities, and density logs using the VFSA method. The hydrate saturation is calculated from chloride anomalies with a background value of ~585 mM using an equation proposed by Malinverno et al. (2008). Since the clay content within the sediments is very high at Site 1326E, a modified Archie's equation (Sava and Hardage, 2007) is used to calculate hydrate saturation from resistivity. The tortuosity factor, cementation exponent and saturation exponent are chosen as 1.0, 2.5 and 2.0, respectively (Riedel et al., 2010a). The clay resistivity is set to be 5 Ωm (Lee and Collett, 2011) and the formation water resistivity is computed using Arps' equation (Arps, 1953) with a pore water salinity of standard sea water, 32 ppt, an assumed seafloor temperature of 3.03 °C and a derived thermal gradient of 60 °C/km (Riedel et al., 2010a). As we can see, the predictions of elastic properties (P- and S-wave velocities, and density) from the GEMM match well with the well-log measurements. The estimated hydrate saturation is consistent with that calculated from the resistivity log in the shallow section (< 160 mbsf), while is slightly overestimated for the intervals between 160 and 250 mbsf compared with those derived from resistivity and chloride data. The latter difference may originate from the absence of density log data for this well, poor borehole conditions (washout) in the deeper section and the different resolutions between sonic and resistivity logs, as well as the lateral variability in gas hydrate distribution. Also, the high percentage of bound water in the clay-rich intervals lowers the resistivity, which leads to the underestimation of gas hydrate saturation. The results show that the average hydrate saturation from 75 to 255 mbsf at U1326 D is 22.13% with a maximum value of 62.22% at 229.85 mbsf. The average inverted fractions of hybrid-cementing, matrix-supporting and pore-filling hydrates are approximately 7%, 34% and 59%, respectively.

6.2.2. IODP expedition 311-hole U1327E

Well-log data from Site U1327E also provide an example of estimating the hydrate saturation and the fractions of hybrid-cementing, matrix-supporting and pore-filling hydrates from elastic properties using the VFSA method (Fig. 11). Here, the hydrate saturation calculated from chloride anomalies is based on a background value of 386 mM (Riedel et al., 2010a). Similarly, the hydrate saturation calculated from resistivity is based on a modified Archie's equation (Sava and Hardage, 2007) with a tortuosity factor of 1.0, a cementation exponent of 2.2 and a saturation exponent of 2.0 (Riedel et al., 2010a). In addition, the formation water resistivity is computed using Arps' equation (Arps, 1953) with a pore water salinity of 24 ppt, an assumed seafloor temperature of 2.95 °C and a derived thermal gradient of 61 °C/km (Riedel et al., 2010a). Results in Fig. 11 show an average hydrate saturation of 7.61% from 150 to 230 mbsf with a maximum value of 40% at 163.82 mbsf. The estimated hydrate saturation is comparable to those from chloride data and resistivity log. The small discrepancy between predicted and referenced values is most likely caused by the absence of density log data, the high clay content, the anisotropic distribution of gas hydrates and the different vertical resolutions for sonic and resistivity logs, as well as degraded borehole conditions. The average inverted fractions of hybrid-cementing, matrix-supporting and pore-filling hydrates are approximately 8%, 32% and 60%, respectively.

6.3. Quantification of hydrate saturation and morphology for terrestrial hydrate-bearing sediments

6.3.1. Mount Elbert test well, Alaska North Slope

We also examine the effectiveness of the GEMM in permafrost-related sediments over a variety of porosities and clay contents at Mount

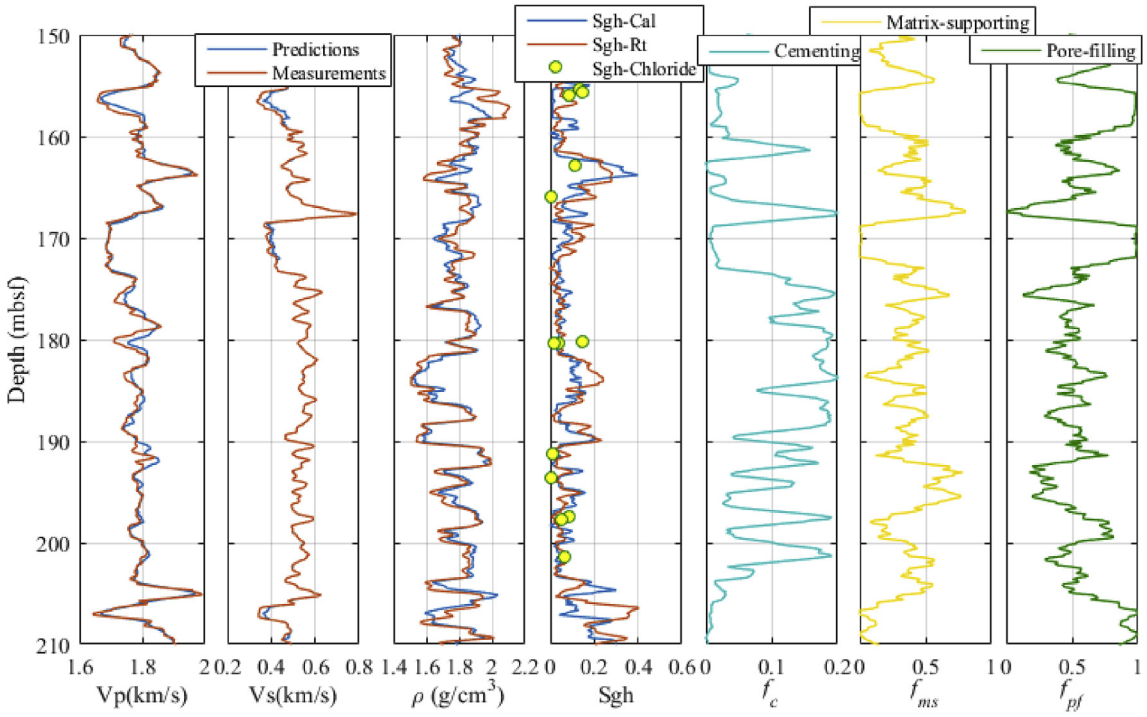

Fig. 11. Inversion results at Site U1327E. From left to right: P-wave and S-wave velocities, density, hydrate saturation, the fractions of hybrid-cementing, matrix-supporting, and pore-filling hydrates. Other legends and symbols are the same as in Fig. 10. All saturations and fractions of hydrate morphologies are smoothed using a 9-point running average.

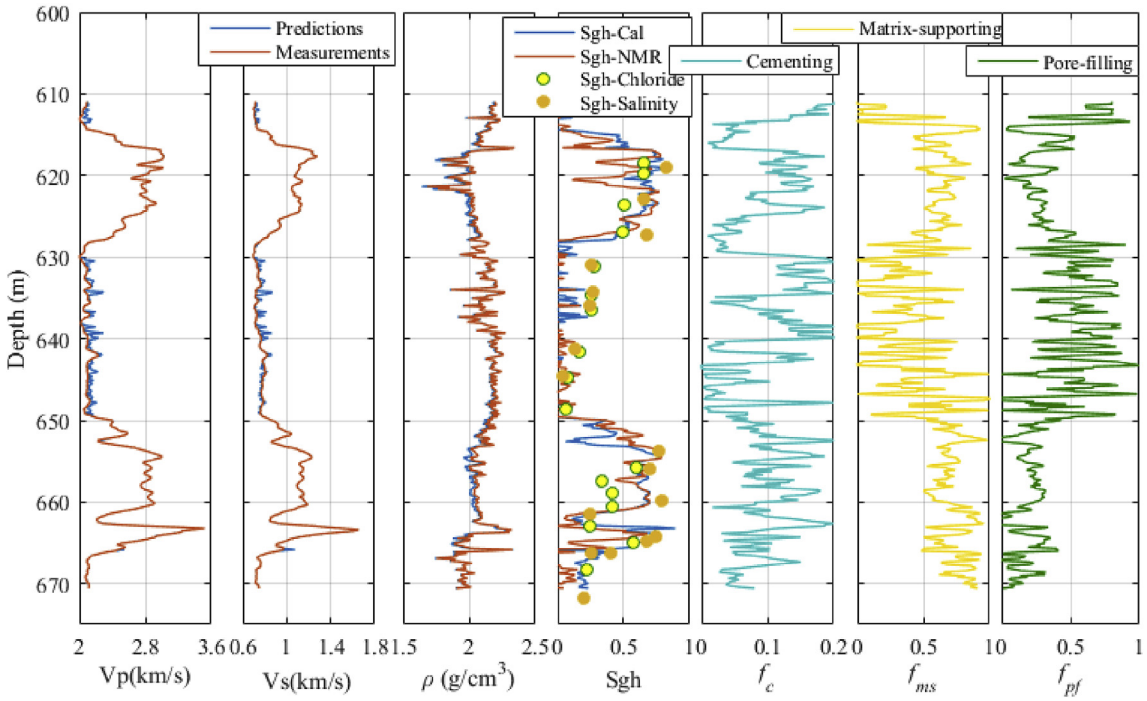

Fig. 12. Inversion results for the Mount Elbert test well. From left to right: P-wave velocity, S-wave velocity, density, hydrate saturation, the fractions of hybrid-cementing, matrix-supporting and pore-filling hydrates. The predication of hydrate saturation from the GEMM is in blue (Sgh-Cal) and the calculation of hydrate saturation from NMR log is in red (Sgh-NMR). The orange dots and the yellow dots denote the hydrate saturation from the salinity (Sgh-Salinity) and chloride (Sgh-Chloride) data, respectively. All saturations and fractions of hydrate morphologies are smoothed using a 5-point running average. (For interpretation of the references to colour in this figure legend, the reader is referred to the Web version of this article.)

Elbert test well site. Fig. 12 shows hydrate saturation and fractions of hydrate morphologies estimated from the P- and S-wave velocities and density logs for depths between 610 and 670 m using the VFSA method. The referenced hydrate saturations are calculated from nuclear magnetic resonance (NMR) log, and analyzed from salinity data and chloride anomalies, respectively. The predicted hydrate saturation varies from 0% to 89% and is comparable to those from the salinity data and the chloride data at the whole intervals and consistent with that

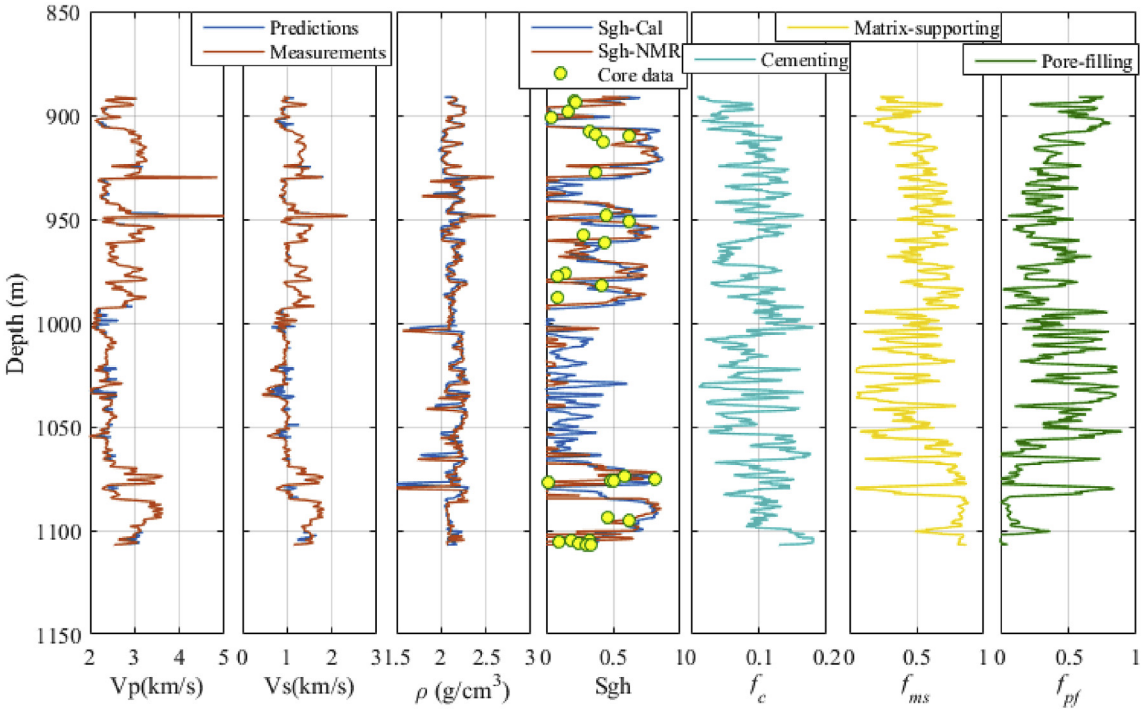

Fig. 13. Inversion results for the Mallik 5L-38 well. From left to right: P-wave velocity, S-wave velocities, density, hydrate saturation, the fractions of hybrid-cementing, matrix-supporting and pore-filling hydrates. The yellow dots denote the hydrate saturation from core data. The predication of hydrate saturation from the GEMM is in blue (Sgh-Cal) and the calculation of hydrate saturation from NMR log is in red (Sgh-NMR). All saturations and fractions of hydrate morphologies are smoothed using a 5-point running average. (For interpretation of the references to colour in this figure legend, the reader is referred to the Web version of this article.)

calculated from the NMR log in the intervals 614–630 m and 649–670.5 m. The inverted average fractions of hybrid-cementing, matrix-supporting and pore-filling hydrates are approximately 10%, 55% and 35%, respectively. This result suggests that hydrates mainly occur as a matrix-supporting form in sand-dominated intervals, whereas they occur as a pore-filling form in the clay-rich intervals.

6.3.2. Mallik 5L-38, Mackenzie Delta

Similarly, acoustic and density logs from the Mallik 5L-38 well are used to estimate three types of hydrate morphological fractions and hydrate saturation corroborated with those from core data and NMR log (Fig. 13). The referenced gas hydrate saturation of nonpressurized cores was determined using the dissociation measurements (Lu et al., 2005). The hydrate saturation calculated from NMR log was based on the method proposed by Kleinberg et al. (2005). The predicted hydrate saturation matches well with those computed from the NMR log, and from core data in hydrate-rich sections ranging from 891 to 991 m and 1067–1107 m, while there is poor agreement between the GEMM prediction and the NMR calculation within clay-rich intervals between 1000 and 1060 m. The discrepancy may be the result of the bound water existing in the clay-rich sediments which weakens the response of NMR log contributed from the pore space occupied by hydrates (Cook and Waite, 2018). The discrepancy between estimated hydrate saturation and that from core samples is ascribed to the underestimation of dissociation measurements from Lu et al. (2005) (Cook and Waite, 2018). The hydrate saturation averages 37.52% with a maximum value up to 92%. The inverted average fractions of hybrid-cementing, matrix-supporting and pore-filling hydrates are approximately 10%, 53% and 37%, respectively. It can be clearly observed that hydrates mainly occur in a pore-filling form at the low hydrate saturation (< 40%) intervals, but in a matrix-supporting form at the high hydrate saturation (> 40%) intervals.

7. Discussion

7.1. Comparison of GEMM with EMM and CCT

Compared with EMM and CCT, our GEMM has several advantages: (1) it overcomes the drawbacks of cementation theory which is independent of effective pressure and is not appropriate to employ in low-porosity sediments; (2) it merges CCT and EMM as it reduces to the EMM when hydrate saturation is zero, and is equivalent to the CCT when the effective pressure tends to zero (see Fig. 5); (3) it can simultaneously account for the impacts of compaction and cementation on the elastic behaviors of consolidated or unconsolidated sediments; (4) it is suitable for characterization of four common hydrate morphologies simultaneously (see Fig. 3) with a common set of modeling parameters (e.g., coordination number and critical porosity, as well as weighted cement factor). The two variable parameters, n and φ_c, can be obtained by fitting the GEMM velocity predictions to the observed P- and S-wave velocities in hydrate-free sediments or calibrated by the fluid substitution method (Pan et al., 2019). An alternative approach for determining the coordination number can be found in Terry and Knapp (2018) and Zhang et al. (2013). The weighted cement factor W_c, not only controls the deposition schemes of the cement, but also provides flexibility by allowing the GEMM to account for diverse combinations of contact-cementing and grain-coating morphologies. For $W_c = 0.5$, the weights of contact-cementing and grain-coating morphologies in the GEMM are equal. For $W_c > 0.5$, the GEMM favors the stiff cement scheme (contact-cementing case) and for $W_c < 0.5$, the model favors the soft cement scheme (grain-coating case). In this study, setting the weighted cement factor as a constant value, instead of allowing it to vary, provides reasonable fits between the measured and predicted velocities, and generates reasonable hydrate saturation estimations. Hence, a lower weighted cement factor of 0.15 ± 0.1 is recommended to use for the “excess-water” (natural) conditions and a moderate value of 0.3 ± 0.1 is recommended for the “excess-gas”

conditions. Generally, the connectivity associated with the permeability, to some extent, dominates the gas supply and migration path which affect the gas hydrate occurrence mechanism. Hence, it would be better to allow for the connectivity between the sediment matrix and hydrates in the model. However, unlike the SCA-DEM model proposed by Jackobsen et al. (2000), Chand et al. (2006) and Minshull and Chand (2009), our model ignores the connectivity due to the usage of modified Hashin-Shtrikman bounds. Moreover, the presented model is not suitable for the case where gas hydrates are present as matrix-inclusion and fracture/vein-filling in the sediments. Hence, future studies will focus on a more complex rock physics modeling strategy which is suitable for simultaneous characterization of six hydrate morphologies as summarized by Dai et al. (2004). Finally, the validation of GEMM in Fig. 5 suggests that it can effectively capture the complex occurrence types and their evolution characteristics during hydrate formation at "excess-gas" and "excess-water" conditions.

7.2. Comparison of synthetic and pressure-core hydrate-bearing sediments

As shown in Figs. 7 and 9, hydrate morphologies obtained from inversion of data from laboratory synthetic and natural hydrate-bearing sediments are completely different. Hydrates formed at the "excess-gas" condition follow an occurrence mode where they initially accumulate at grain contacts or evenly coat grain surfaces (< 10% hydrate saturation), and then fill pore space with increasing hydrate saturation (< 40%). However, hydrates grown at the "excess-water" condition (e.g. natural environment) quickly occupy the pore space, and increasingly become part of the frame (~60% hydrate saturation). Overall, there exists a transition of hydrate morphology from hybrid-cementing to pore-filling or from pore-filling to matrix-supporting, but there is no clear boundary between these morphologies. Therefore, it is necessary to conduct extensive laboratory experiments to investigate the evolution of gas hydrate morphology.

7.3. Comparison of hydrate occurrences in marine and terrestrial sediments

Hydrate saturation and fractional morphologies were predicted for gas hydrate-bearing sediments in both marine and terrestrial permafrost settings. As shown in Figs. 10–13, the calculated P- and S-wave velocities and density agree well with the measured values and the predicted hydrate saturations are consistent with those obtained from core data and/or NMR log, which validates the feasibility and applicability of the GEMM.

Table 4 summarizes the statistics of estimated hydrate saturations and fractions of morphologies at the selected four sites. The maximum/average hydrate saturations at Hole U1326D and Hole U1327E are much less than those at Mount Elbert and Mallik 5L-38. This indicates that large amounts of gas hydrates (commonly 27.90–37.52%, locally up to 89–92%) are typically present in coarse-grained terrestrial sediments, whereas small or moderate amounts of gas hydrates (up to 40–62.2% but averaging roughly 7.6–22.13%) are preferentially present in fine-grained marine sediments. Gas hydrates in marine sediments predominantly occur as a pore-filling form (averaging about 59%), whereas in terrestrial sediments they exist mainly as a matrix-supporting form (averaging about 54%). Moreover, it is found that the hybrid-cementing hydrate saturation in terrestrial sediments is higher than that in marine sediments. Furthermore, the hybrid-cementing hydrates are more likely to be occurred at the deep section of GHSZ instead of the shallow section as shown in Figs. 10–13, especially for the marine environments. This is most likely associated with well permeable migration pathway and adequate gas supply which is conducive to form excess-gas systems locally. This finding will be helpful for better understanding the occurrence mechanism of cementing hydrates in natural environments.

Overall, the coarse-grained terrestrial sediments may possess high-saturation matrix-supporting hydrates, whereas the fine-grained marine sediments may contain low-saturation pore-filling hydrates. In addition, it is observed that hydrates preferentially occur as hybrid-cementing morphology in the deeper section of GHSZ with high hydrate saturation.

7.4. Analysis of inversion results

The GEMM-based hydrate saturation results are validated by their similarity to those calculated from core data and resistivity and/or NMR logs. However, to strengthen the results, laboratory experiments and digital rock physics modeling should be carried out on more samples of synthetic and natural hydrate-bearing sediments to examine gas hydrate morphologies. Due to limited input data (P- and S-wave velocities and density), the developed model can be used to quantify at most four hydrate morphologies. Hence, other hydrate-morphology-dependent geophysical properties, such as seismic wave attenuation, resistivity, shear strength and permeability, should be integrated when evaluating more complex hydrate morphologies. Our GEMM model not only provides some insights into the pore-scale occurrence mechanism of gas hydrates, but also lays a theoretical foundation for laboratory experiments and paves the way for successful quantifications of hydrate saturation and morphology from conventional seismic surveys.

8. Conclusions

In this study, we propose a generalized effective medium model (GEMM) by utilizing a modified cementation theory based on approximate expressions of the stiffnesses with the newly derived pressure-dependent normalized contact-cemented radii. Validation of the GEMM against laboratory data for synthetic methane and THF hydrates suggests that this model not only can account for four types of hydrate morphologies, such as contact-cementing, grain-coating, matrix-supporting and pore-filling, separately or jointly, but also can capture the evolution characteristics of hydrate morphology during hydrate formation. Quantification of the fractions of hydrate morphologies for laboratory synthetic and natural hydrate samples confirms the completely different patterns of hydrate occurrence in "gas-excess" and "water-excess" environments. Finally, gas hydrate saturation and fractions of matrix-supporting, pore-filling and hybrid-cementing morphologies are inverted simultaneously from the sonic and density logs measured at the northern Cascadia margin, Alaska North Slope, and Mackenzie Delta. The good agreement between the predicted hydrate saturations and those derived from core data and resistivity or NMR logs demonstrates the broad applicability of our model. Also, our estimations suggest that gas hydrates preferentially occur as matrix-supporting morphology in sand-dominated terrestrial sediments,

Table 4
Statistics of estimated hydrate saturations and fractions of possible morphologies at four sites. (max = maximum; avg = average).

Regions	Sites	Hydrate saturation (max)	Hydrate saturation (avg)	Hybrid- Cementing (avg)	Matrix- Supporting (avg)	Pore- filling (avg)
Marine	U1326D	62.2%	22.13%	7%	34%	59%
	U1327E	40%	7.61%	8%	32%	60%
Terrestrial	Mount Elbert	89%	27.90%	10%	55%	35%
	Mallik 5L-38	92%	37.52%	10%	53%	37%

whereas they exhibit pore-filling morphology in clay-rich marine sediments. Specifically, cementing hydrates are prone to grow in the deeper section of GHSZ.

Author contribution statement

Haojie Pan: Developing generalized effective medium theory, programming and testing the code, writing original draft and revising the paper. Hongbing Li: Supervision, providing insights into developing generalized effective medium theory, discussing the outline of the paper, reviewing and revising the paper. Jingyi Chen: Supervision, reviewing and revising the paper. Michael Riedel: Choosing well-log data, discussing the usage of well-log data and modeling and inversion schemes, reviewing and revising the paper. Melanie Holland: Discussing the hydrate occurrence mechanism and the usage of experimental data, reviewing and revising the paper. Yan Zhang: Supervision, reviewing and revising the manuscript. Shengjuan Cai: Processing well-log data, drawing Figs. 2–4, reviewing and revising the manuscript.

Declaration of competing interests

None.

Acknowledgements

This work is supported by the Scientific Research & Technology Development Project of China National Petroleum Corporation (Grant No. 2017D-3504), Basic Research and Strategic Reserve Technology Funds for Affiliated Institutions of China National Petroleum Corporation (2018D-500811) and China Scholarship Council (201805150004). We would like to thank Dr. Dugarov for sharing the experimental data. We are especially thankful to Dr. Karl Lang and Dr. Scott Dallimore for sharing the well logging data. Special acknowledgements are extended to the Mount Elbert science party and the scientists and personnel associated with the Mallik and IODP Expedition 311 projects. We also appreciate the Associate Editor Daniel Praeg, Dr. Ray Boswell, Dr. Urmi Majumdar and an anonymous reviewer for their helpful comments and suggestions that improve the quality of the paper. Finally, we are also grateful to Research Institute of Petroleum Exploration and Development for permission to publish this work.

Appendix A. Supplementary data

Supplementary data to this article can be found online at https://doi.org/10.1016/j.marpetgeo.2019.104166.

Nomenclature

a	Contact-cementation radius
a_0	Initial contact radius
b	Classic contact-cementation radius
D_N	Normal stiffness in the “rigid cement” regime
D_T	Tangential stiffness in the “rigid cement” regime
E_i	Initial error (or energy)
E_j	Updated error (or energy)
f_c	Fraction of the cementing hydrates
f_h	Fraction of matrix-supporting hydrates in the matrix
f_{ms}	Fraction of matrix-supporting hydrates
f_{pf}	Fraction of pore-filling hydrates
G_{cct}	Effective shear modulus at the critical porosity
G_{dry}	Shear modulus of dry rock
G_h	Shear modulus of gas hydrates
G_{ma}	Shear modulus of the matrix
G_s	Shear modulus of sand
G_{sat}	Shear modulus of saturated rock
G_{sh}	Shear modulus of shale
i	Previous iteration number
j	Subsequent iteration number
k	Intermediate iteration number
K_{cct}	Effective bulk modulus at the critical porosity
K_{dry}	Bulk modulus of dry rock
K_{fl}	Bulk modulus of pore fluid
K_h	Bulk modulus of gas hydrates
K_{ma}	Bulk modulus of the matrix
K_w	Bulk modulus of water
K_s	Bulk modulus of sand
K_{sat}	Bulk modulus of saturated rock
K_{sh}	Bulk modulus of clay
m_i	Initial model
m_j	Updated model
n	Coordination number
N_T	Total number of iterations
p	Accepted probability
P_{eff}	Effective pressure
R	Spherical grain radius
S_c	Hybrid-cementing hydrate saturation
S_{gh}	Total hydrate saturation
S_N	Normal stiffness
S_T	Tangential stiffness
T_0	Initial temperature
T_k	Temperature at the kth iteration
u_i	A random number varying between 0 and 1
V_p^{obs}	Observed P-wave velocity
V_p^{cal}	Calculated P-wave velocity
V_s^{obs}	Observed S-wave velocity
V_s^{cal}	Calculated S-wave velocity
V_{sh}	Clay (or shale) content
W_c	Weighted cement factor
y_i	The perturbation term
α	Pressure-dependent contact-cementation radius
α_0	Initial normalized contact radius
β	Classic normalized cement radii
λ	A parameter used to control the temperature schedule
φ	Sediment porosity
φ_e	The reduced porosity due to the presence of matrix-supporting hydrates
φ_c	Critical porosity
φ_{eff}	Effective porosity
ν_{ma}	Poisson's ratio of the matrix
ν_h	Poisson's ratio of the hydrates
ρ_b^{obs}	Observed bulk density
ρ_b^{cal}	Calculated bulk density

References

Allo, F., 2019. Consolidating rock-physics classics: a practical take on granular effective medium models. Lead. Edge 38 (5), 334–340.

Arps, J.J., 1953. The effect of temperature on the density and electrical resistivity of sodium chloride solutions. J. Pet. Technol. 5 (10), 17–20.

Best, A.I., Priest, J.A., Clayton, C.R., Rees, E.V., 2013. The effect of methane hydrate morphology and water saturation on seismic wave attenuation in sand under shallow sub-seafloor conditions. Earth Planet. Sci. Lett. 368, 78–87. https://doi.org/10.1016/j.epsl.2013.02.033.

Chand, S., Minshull, T.A., Gei, D., Carcione, J.M., 2004. Elastic velocity models for gas-hydrate-bearing sediments-A comparison. Geophys. J. Int. 159 (2), 573–590. https://doi.org/10.1111/j.1365-246X.2004.02387.x.

Chand, S., Minshull, T.A., Priest, J.A., Best, A.I., Clayton, C.R., Waite, W.F., 2006. An effective medium inversion algorithm for gas hydrate quantification and its application to laboratory and borehole measurements of gas hydrate-bearing sediments. Geophys. J. Int. 166 (2), 543–552. https://doi.org/10.1111/j.1365-246X.2006.03038.x.

Chaouachi, M., Falenty, A., Sell, K., Enzmann, F., Kersten, M., Haberthür, D., Kuhs, W.F., 2015. Microstructural evolution of gas hydrates in sedimentary matrices observed with synchrotron X-ray computed tomographic microscopy. Geochem. Geophys. Geosyst. 16 (6), 1711–1722. https://doi.org/10.1002/2015GC005811.

Collett, T.S., Boswell, R., Waite, W.F., Kumar, P., Roy, S.K., Chopra, K., Singh, S.K., Yamada, Y., Tenma, N., Pohlman, J., Zyrianova, M., 2019. India National Gas Hydrate Program Expedition 02 summary of scientific results: gas hydrate systems along the eastern continental margin of India. Mar. Pet. Geol. https://doi.org/10.1016/j.marpetgeo.2019.05.023.

Cook, A.E., Goldberg, D.S., Malinverno, A., 2014. Natural gas hydrates occupying fractures: a focus on non-vent sites on the Indian continental margin and the northern Gulf of Mexico. Mar. Pet. Geol. 58, 278–291. https://doi.org/10.1016/j.marpetgeo.2014.04.013.

Cook, A.E., Waite, W.F., 2018. Archie's saturation exponent for natural gas hydrate in coarse-grained reservoirs. J. Geophys. Res.: Solid Earth 123 (3), 2069–2089. https://doi.org/10.1002/2017JB015138.

Cortes, D.D., Martin, A.I., Yun, T.S., Francisca, F.M., Santamarina, J.C., Ruppel, C., 2009. Thermal conductivity of hydrate-bearing sediments. J. Geophys. Res.: Solid Earth 114 (B11). https://doi.org/10.1029/2008JB006235.

Dai, J., Snyder, F., Gillespie, D., Koesoemadinata, A., Dutta, N., 2008. Exploration for gas hydrates in the deepwater, northern Gulf of Mexico: Part I. A seismic approach based on geologic model, inversion, and rock physics principles. Mar. Pet. Geol. 25 (9), 830–844. https://doi.org/10.1016/j.marpetgeo.2008.02.006.

Dai, J., Xu, H., Snyder, F., Dutta, N., 2004. Detection and estimation of gas hydrates using rock physics and seismic inversion: examples from the northern deep-water Gulf of Mexico. Lead. Edge 23 (1), 60–66. https://doi.org/10.1190/1.1645456.

Dai, S., Santamarina, J.C., 2014. Sampling disturbance in hydrate-bearing sediment pressure cores: NGHP-01 expedition, Krishna-Godavari Basin example. Mar. Pet. Geol. 58, 178–186. https://doi.org/10.1016/j.marpetgeo.2014.07.013.

Dai, S., Santamarina, J.C., Waite, W.F., Kneafsey, T.J., 2012. Hydrate morphology: physical properties of sands with patchy hydrate saturation. J. Geophys. Res.: Solid Earth 117 (B11). https://doi.org/10.1029/2012JB009667.

Dallimore, S.R., Collett, T.S., 2005. Scientific Results from the Mallik 2002 Gas Hydrate Production Research Well Program, Mackenzie Delta, Northwest Territories, Canada, 585. Geological Survey of Canada, Bullitin, Canada, Ottawa, pp. 1–36.

Delli, M.L., Grozic, J.L., 2014. Experimental determination of permeability of porous media in the presence of gas hydrates. J. Pet. Sci. Eng. 120, 1–9. https://doi.org/10.1016/j.petrol.2014.05.011.

Digby, P.J., 1981. The effective elastic moduli of porous granular rocks. J. Appl. Mech. 48 (4), 803–808. https://doi.org/10.1115/1.3157738.

Dugarov, G.A., Duchkov, A.A., Duchkov, A.D., Drobchik, A.N., 2019. Laboratory validation of effective acoustic velocity models for samples bearing hydrates of different type. J. Nat. Gas Sci. Eng. 63, 38–46. https://doi.org/10.1016/j.jngse.2019.01.007.

Dvorkin, J., Yin, H., 1995. Contact laws for cemented grains: implications for grain and cement failure. Int. J. Solids Struct. 32 (17–18), 2497–2510. https://doi.org/10.1016/0020-7683(94)00279-6.

Dvorkin, J., Nur, A., 1996. Elasticity of high-porosity sandstones: theory for two North Sea data sets. Geophysics 61 (5), 1363–1370. https://doi.org/10.1190/1.1444059.

Dvorkin, J., Prasad, M., Sakai, A., Lavoie, D., 1999. Elasticity of marine sediments: rock physics modeling. Geophys. Res. Lett. 26 (12), 1781–1784. https://doi.org/10.1029/1999GL900332.

Ecker, C., Dvorkin, J., Nur, A., 1998. Sediments with gas hydrates: internal structure from seismic AVO. Geophysics 63 (5), 1659–1669. https://doi.org/10.1190/1.1444462.

Elata, D., Dvorkin, J., 1996. Pressure sensitivity of cemented granular materials. Mech. Mater. 23 (2), 147–154. https://doi.org/10.1016/0167-6636(96)00005-1.

Ellis, M.H., 2008. Joint Seismic and Electrical Measurements of Gas Hydrates in Continental Margin Sediments. Doctoral dissertation. University of Southampton, UK.

Gassmann, F., 1951. Elastic waves through a packing of spheres. Geophysics 16 (4), 673–685. https://doi.org/10.1190/1.1437718.

Hashin, Z., Shtrikman, S., 1963. A variational approach to the theory of the elastic behavior of multiphase materials. J. Mech. Phys. Solids 11 (2), 127–140. https://doi.org/10.1016/0022-5096(63)90060-7.

Helgerud, M.B., 2001. Wave Speeds in Gas Hydrate and Sediments Containing Gas Hydrate: A Laboratory and Modeling Study. Doctoral dissertation. Stanford University, USA.

Helgerud, M.B., Dvorkin, J., Nur, A., Sakai, A., Collett, T., 1999. Elastic-wave velocity in marine sediments with gas hydrates: effective medium modeling. Geophys. Res. Lett. 26 (13), 2021–2024. https://doi.org/10.1029/1999GL900421.

Henninges, J., Huenges, E., Burkhardt, H., 2005. In situ thermal conductivity of gas hydrate-bearing sediments of the Mallik 5L-38 well. J. Geophys. Res.: Solid Earth 110 (B11). https://doi.org/10.1029/2005JB003734.

Hill, R., 1963. Elastic properties of reinforced solids: some theoretical principles. J. Mech. Phys. Solids 11 (5), 357–372. https://doi.org/10.1016/0022-5096(63)90036-X.

Holland, M.E., Schultheiss, P., Roberts, J., Druce, M., 2008. Observed gas hydrate morphologies in marine sediments. In: 6th International Conference on Gas Hydrates, Chevron, Vancouver, BC, Canada, pp. 6–10.

Holland, M.E., Schultheiss, P.J., Roberts, J.A., 2018. Gas hydrate saturation and morphology from analysis of pressure cores acquired in the Bay of Bengal during expedition NGHP-02, offshore India. Mar. Pet. Geol. https://doi.org/10.1016/j.marpetgeo.2018.07.018.

Hu, G.W., Ye, Y.G., Zhang, J., Diao, S.B., Liu, C.L., 2012. Acoustic properties of hydrate-bearing unconsolidated sediments measured by the bender element technique. Chin. J. Geophys. 55 (6), 635–647. https://doi.org/10.1002/cjg2.1758.

Ingber, L., 1989. Very fast simulated re-annealing. Math. Comput. Model. 12 (8), 967–973. https://doi.org/10.1016/0895-7177(89)90202-1.

Jaiswal, P., Al-Bulushi, S., Dewangan, P., 2014. Logging-while-drilling and wireline velocities: Site NGHP-01-10, Krishna–Godavari Basin, India. Marine and Petroleum Geology 58, 331–338.

Jakobsen, M., Hudson, J.A., Minshull, T.A., Singh, S.C., 2000. Elastic properties of hydrate-bearing sediments using effective medium theory. J. Geophys. Res.: Solid Earth 105 (B1), 561–577. https://doi.org/10.1029/1999JB900190.

Jin, Y., Konno, Y., Yoneda, J., Kida, M., Nagao, J., 2016. In situ methane hydrate morphology investigation: natural gas hydrate-bearing sediment recovered from the Eastern Nankai Trough Area. Energy Fuels 30 (7), 5547–5554. https://doi.org/10.1021/acs.energyfuels.6b00762.

Katagiri, J., Konno, Y., Yoneda, J., Tenma, N., 2017. Pore-scale modeling of flow in particle packs containing grain-coating and pore-filling hydrates: verification of a Kozeny-Carman-based permeability reduction model. J. Nat. Gas Sci. Eng. 45, 537–551. https://doi.org/10.1016/j.jngse.2017.06.019.

Kim, G.Y., Narantsetseg, B., Ryu, B.J., Yoo, D.G., Lee, J.Y., Kim, H.S., Riedel, M., 2013. Fracture orientation and induced anisotropy of gas hydrate-bearing sediments in seismic chimney-like-structures of the Ulleung Basin, East Sea. Mar. Pet. Geol. 47, 182–194. https://doi.org/10.1016/j.marpetgeo.2013.06.001.

Kingston, E., Clayton, C., Priest, J., 2008. Gas hydrate growth morphologies and their effect on the stiffness and damping of a hydrate bearing sand. In: 6th International Conference on Gas Hydrate. British Columbia, Canada.

Kleinberg, R.L., Flaum, C., Collett, T.S., 2005. Magnetic resonance log of JAPEX/JNOC/GSC et al. Mallik 5L-38 gas hydrate production research well: gas hydrate saturation, growth habit, and relative permeability. Bull. Geol. Surv. Can. 585, 114.

Langlois, V., 2015. Elastic behavior of weakly cemented contact. Int. J. Numer. Anal. Methods Geomech. 39 (8), 854–860. https://doi.org/10.1002/nag.2342.

Lee, J.Y., Yun, T.S., Santamarina, J.C., Ruppel, C., 2007. Observations related to tetrahydrofuran and methane hydrates for laboratory studies of hydrate-bearing sediments. Geochem. Geophys. Geosyst. 8 (6). https://doi.org/10.1029/2006GC001531.

Lee, M.W., 2002. Biot-Gassmann theory for velocities of gas hydrate-bearing sediments. Geophysics 67 (6), 1711–1719. https://doi.org/10.1190/1.1527072.

Lee, M.W., Collett, T.S., 2009. Gas hydrate saturations estimated from fractured reservoir at Site NGHP-01-10, Krishna-Godavari Basin, India. J. Geophys. Res.: Solid Earth 114 (B7). https://doi.org/10.1029/2008JB006237.

Lee, M.W., Collett, T.S., 2011. In-situ gas hydrate hydrate saturation estimated from various well logs at the Mount Elbert gas hydrate stratigraphic test well, Alaska North Slope. Mar. Pet. Geol. 28 (2), 439–449. https://doi.org/10.1016/j.marpetgeo.2009.06.007.

Lee, M.W., Hutchinson, D.R., Collett, T.S., Dillon, W.P., 1996. Seismic velocities for hydrate-bearing sediments using weighted equation. J. Geophys. Res.: Solid Earth 101 (B9), 20347–20358. https://doi.org/10.1029/96JB01886.

Lee, M.W., Waite, W.F., 2008. Estimating pore-space gas hydrate saturations from well log acoustic data. Geochem. Geophys. Geosyst. 9 (7). https://doi.org/10.1029/2008GC002081.

Liu, X., Yin, X., Luan, X., 2018. Seismic rock physical modelling for gas hydrate-bearing sediments. Sci. China Earth Sci. 61 (9), 1261–1278. https://doi.org/10.1007/s11430-017-9214-2.

Liu, Z., Dai, S., Ning, F., Peng, L., Wei, H., Wei, C., 2018. Strength estimation for hydrate-bearing sediments from direct shear tests of hydrate-bearing sand and silt. Geophys. Res. Lett. 45 (2), 715–723. https://doi.org/10.1002/2017GL076374.

Lu, H., Dutrisac, R., Ripmeester, J., Wright, F., Uchida, T., 2005. Measurements of gas hydrate saturation in sediment cores recovered from the JAPEX/JNOC/GSC et al. Mallik 5L-38 gas hydrate production research well. Bull. Geol. Surv. Can. 585, 89.

Malinverno, A., Kastner, M., Torres, M.E., Wortmann, U.G., 2008. Gas hydrate occurrence from pore water chlorinity and downhole logs in a transect across the northern Cascadia margin (Integrated Ocean Drilling Program Expedition 311). J. Geophys. Res.: Solid Earth 113 (B8). https://doi.org/10.1029/2008JB005702.

Marín-Moreno, H., Sahoo, S.K., Best, A.I., 2017. Theoretical modeling insights into elastic wave attenuation mechanisms in marine sediments with pore-filling methane hydrate. J. Geophys. Res.: Solid Earth 122 (3), 1835–1847. https://doi.org/10.1002/2016JB013577.

Mavko, G., Mukerji, T., Dvorkin, J., 2009. The Rock Physics Handbook: Tools for Seismic Analysis of Porous Media. Cambridge university press.

Mindlin, R.D., 1949. Compliance of elastic bodies in contact. J. Appl. Mech., ASME 16, 259–268. https://ci.nii.ac.jp/naid/10013415139/.

Minshull, T.A., Chand, S., 2009. The pore-scale distribution of sediment-hosted hydrates: evidence from effective medium modelling of laboratory and borehole seismic data. Geol. Soc., Lond., Spec. Publ. 319 (1), 93–101. https://doi.org/10.1144/SP319.8.

Nguyen-Sy, T., Tang, A.M., To, Q.D., Vu, M.N., 2019. A model to predict the elastic properties of gas hydrate-bearing sediments. J. Appl. Geophys. 169, 154–164. https://doi.org/10.1016/j.jappgeo.2019.05.003.

Pan, H.J., Li, H.B., Chen, J.Y., Zhang, Y., Cai, S.J., Huang, Y.C., Zheng, Y., Zhao, Y., Deng, J., 2019a. A unified contact cementation theory for gas hydrate morphology detection and saturation estimation from elastic-wave velocities. Mar. Pet. Geol. https://doi.org/10.1016/j.marpetgeo.2019.104146.

Pan, H.J., Li, H.B., Chen, J.Y., Zhang, Y., Liu, X.B., Cai, S.J., Cao, C.J., 2019b. Evaluation of gas hydrate resources using hydrate morphology-dependent rock physics templates. J. Pet. Sci. Eng. https://doi.org/10.1016/j.petrol.2019.106268.

Pan, H.J., Li, H.B., Grana, D., Zhang, Y., Liu, T.Y., Geng, C., 2019c. Quantitative characterization of gas hydrate bearing sediment using elastic-electrical rock physics models. Mar. Pet. Geol. 105, 273–283. https://doi.org/10.1016/j.marpetgeo.2019.04.034.

Pan, H.J., Li, H.B., Zhang, Y., Cai, S.J., 2019d. 3D elastic-electrical rock physics template inversion for reservoir parameters of gas hydrate bearing sediment. In: 81st EAGE Conference and Exhibition 2019, https://doi.org/10.3997/2214-4609.201901639.

Priest, J.A., Best, A.I., Clayton, C.R., 2005. A laboratory investigation into the seismic velocities of methane gas hydrate-bearing sand. J. Geophys. Res.: Solid Earth 110 (B4). https://doi.org/10.1029/2004JB003259.

Priest, J.A., Best, A.I., Clayton, C.R., 2006. Attenuation of seismic waves in methane gas hydrate-bearing sand. Geophys. J. Int. 164 (1), 149–159. https://doi.org/10.1111/j.

1365-246X.2005.02831.x.
Qian, J., Wang, X., Collett, T.S., Dong, D., Guo, Y., Su, P., Liang, J., 2017. Gas hydrate accumulation and saturations estimated from effective medium theory in the eastern Pearl River Mouth Basin, South China Sea. Interpretation 5 (3), SM33–SM48. https://doi.org/10.1190/INT-2016-0217.1.
Riedel, M., Collett, T.S., Malone, M., 2006. The expedition 311 scientists. In: Proc. IODP, vol. 311 Integrated Ocean Drilling Program Management International. Inc., Washinton, DC.
Riedel, M., Collett, T.S., Malone, M., the Expedition 311 Scientists, 2010a. Expedition 311 synthesis: scientific findings. In: Proc. IODP 311 Integrated Ocean Drilling Program Management International. Inc., Washinton, DC.
Riedel, M., Goldberg, D., Guerin, G., 2014. Compressional and shear-wave velocities from gas hydrate bearing sediments: examples from the India and Cascadia margins as well as Arctic permafrost regions. Mar. Pet. Geol. 58, 292–320. https://doi.org/10.1016/j.marpetgeo.2014.07.028.
Riedel, M., Willoughby, E.C., Chopra, S. (Eds.), 2010. Geophysical Characterization of Gas Hydrates. Society of Exploration Geophysicists, Tulsa, Oklahoma, pp. 1–22.
Rydzy, M.B., 2014. The Effect of Hydrate Formation on the Elastic Properties of Unconsolidated Sediment. PhD dissertation. Colorado School of Mines, Colorado, USA.
Sahoo, S.K., Marín-Moreno, H., North, L.J., Falcon-Suarez, I., Madhusudhan, B.N., Best, A.I., Minshull, T.A., 2018. Presence and consequences of coexisting methane gas with hydrate under two phase water-hydrate stability conditions. J. Geophys. Res.: Solid Earth 123 (5), 3377–3390. https://doi.org/10.1029/2018JB015598.
Sahoo, S.K., North, L.J., Marín-Moreno, H., Minshull, T.A., Best, A.I., 2019. Laboratory observations of frequency-dependent ultrasonic P-wave velocity and attenuation during methane hydrate formation in Berea sandstone. Geophys. J. Int. 219 (1), 713–723. https://doi.org/10.1093/gji/ggz311.
Sava, D.C., Hardage, B.A., 2007. Gas-hydrate Concentration and Uncertainty Estimation from Electrical-Resistivity Logs: Examples from Green Canyon, Gulf of Mexico. 77th SEG Technical Program Expanded Abstracts, pp. 1579–1583.
Schindler, M., Batzle, M.L., Prasad, M., 2017. Micro X-Ray computed tomography imaging and ultrasonic velocity measurements in tetrahydrofuran-hydrate-bearing sediments. Geophys. Prospect. 65, 1025–1036. https://doi.org/10.1111/1365-2478.12449.
Sloan Jr., E.D., 1998. Clathrate Hydrates of Natural Gases, second ed. Marcel Dekker Inc, New York.
Sriram, G., Dewangan, P., Ramprasa, T., 2014. Modified effective medium model for gas hydrate bearing, clay-dominated sediments in the Krishna–Godavari Basin. Marine and Petroleum Geology 58, 321–330.
Terry, D.A., Knapp, C.C., 2018. A unified effective medium model for gas hydrates in sediments. Geophysics 83 (6), MR317–MR332. https://doi.org/10.1190/geo2017-0513.1.
Winkler, K.W., 1983. Contact stiffness in granular porous materials: comparison between theory and experiment. Geophys. Res. Lett. 10 (11), 1073–1076. https://doi.org/10.1029/GL010i011p01073.
Winters, W.J., Dallimore, S.R., Collett, T.S., Medioli, B.E., Matsumoto, R., Katsube, T.J., Brennan-Alpert, P., 2005. Relationships of sediment physical properties from the JAPEX/JNOC/GSC et al. Mallik 5L-38 gas hydrate production research well. Bull. Geol. Surv. Can. 585, 84.
Winters, W.J., Walker, M., Hunter, R., Collett, T., Boswell, R., Rose, K., Waite, W., Torres, M., Patil, S., Dandekar, A., 2011. Physical properties of sediment from the Mount Elbert gas hydrate stratigraphic test well, Alaska North Slope. Mar. Pet. Geol. 28 (2), 361–380. https://doi.org/10.1016/j.marpetgeo.2010.01.008.
Winters, W.J., Wilcox-Cline, R.W., Long, P., Dewri, S.K., Kumar, P., Stern, L., Kerr, L., 2014. Comparison of the physical and geotechnical properties of gas-hydrate-bearing sediments from offshore India and other gas-hydrate-reservoir systems. Mar. Pet. Geol. 58, 139–167. https://doi.org/10.1016/j.marpetgeo.2014.07.024.
Yang, L., Falenty, A., Chaouachi, M., Haberthür, D., Kuhs, W.F., 2016. Synchrotron X-ray computed microtomography study on gas hydrate decomposition in a sedimentary matrix. Geochem. Geophys. Geosyst. 17 (9), 3717–3732. https://doi.org/10.1002/2016GC006521.
Yoneda, J., Oshima, M., Kida, M., Kato, A., Konno, Y., Jin, Y., Jang, J., Waite, W., Kumar, P., Tenma, N., 2018a. Pressure core based onshore laboratory analysis on mechanical properties of hydrate-bearing sediments recovered during India's National Gas Hydrate Program Expedition (NGHP) 02. Mar. Pet. Geol. https://doi.org/10.1016/j.marpetgeo.2018.09.005.
Yoneda, J., Oshima, M., Kida, M., Kato, A., Konno, Y., Jin, Y., Tenma, N., 2018b. Consolidation and hardening behavior of hydrate-bearing pressure-core sediments recovered from the Krishna–Godavari Basin, offshore India. Mar. Pet. Geol. https://doi.org/10.1016/j.marpetgeo.2018.09.021.
Yoneda, J., Oshima, M., Kida, M., Kato, A., Konno, Y., Jin, Y., Tenma, N., 2018c. Permeability variation and anisotropy of gas hydrate-bearing pressure-core sediments recovered from the Krishna–Godavari Basin, offshore India. Mar. Pet. Geol. https://doi.org/10.1016/j.marpetgeo.2018.07.006.
Zhang, Z., Han, D.H., McConnell, D.R., 2013. Characterization of elastic properties of near-surface and subsurface deepwater hydrate-bearing sediments. Geophysics 78 (3), D169–D179. https://doi.org/10.1190/geo2012-0385.1.